TU Delft

Delft University of Technology

Extrusion-based 3D printing of ex situ-alloyed highly biodegradable MRI-friendly porous iron-manganese scaffolds

Putra, N. E.; Leeflang, M. A.; Taheri, P.; Fratila-Apachitei, L. E.; Mol, J. M.C.; Zhou, J.; Zadpoor, A. A.

DOI
10.1016/j.actbio.2021.07.042

Publication date
2021

Document Version
Final published version

Published in
Acta Biomaterialia

Citation (APA)
Putra, N. E., Leeflang, M. A., Taheri, P., Fratila-Apachitei, L. E., Mol, J. M. C., Zhou, J., & Zadpoor, A. A. (2021). Extrusion-based 3D printing of ex situ-alloyed highly biodegradable MRI-friendly porous iron-manganese scaffolds. *Acta Biomaterialia*, *134*, 774-790. https://doi.org/10.1016/j.actbio.2021.07.042

Important note
To cite this publication, please use the final published version (if applicable).
Please check the document version above.

Copyright
Other than for strictly personal use, it is not permitted to download, forward or distribute the text or part of it, without the consent of the author(s) and/or copyright holder(s), unless the work is under an open content license such as Creative Commons.

Takedown policy
Please contact us and provide details if you believe this document breaches copyrights.
We will remove access to the work immediately and investigate your claim.

This work is downloaded from Delft University of Technology.
For technical reasons the number of authors shown on this cover page is limited to a maximum of 10.

Acta Biomaterialia 134 (2021) 774–790

Contents lists available at ScienceDirect

Acta Biomaterialia

journal homepage: www.elsevier.com/locate/actbio

Full length article

Extrusion-based 3D printing of *ex situ*-alloyed highly biodegradable MRI-friendly porous iron-manganese scaffolds

N.E. Putra[a,*], M.A. Leeflang[a], P. Taheri[b], L.E. Fratila-Apachitei[a], J.M.C. Mol[b], J. Zhou[a], A.A. Zadpoor[a]

[a] Department of Biomechanical Engineering, Faculty of Mechanical, Maritime, and Materials Engineering, Delft University of Technology, Mekelweg 2, Delft 2628 CD, the Netherlands
[b] Department of Materials Science and Engineering, Faculty of Mechanical, Maritime, and Materials Engineering, Delft University of Technology, Mekelweg 2, Delft 2628 CD, the Netherlands

ARTICLE INFO

Article history:
Received 26 May 2021
Revised 20 July 2021
Accepted 20 July 2021
Available online 24 July 2021

Keywords:
3D printing
Material extrusion
Biodegradable
Iron-manganese
Scaffold
Bone substitution

ABSTRACT

Additively manufactured biodegradable porous iron has been only very recently demonstrated. Two major limitations of such a biomaterial are very low biodegradability and incompatibility with magnetic resonance imaging (MRI). Here, we present a novel biomaterial that resolves both of those limitations. We used extrusion-based 3D printing to fabricate *ex situ*-alloyed biodegradable iron-manganese scaffolds that are non-ferromagnetic and exhibit enhanced rates of biodegradation. We developed ink formulations containing iron and 25, 30, or 35 wt% manganese powders, and debinding and sintering process to achieve Fe-Mn scaffolds with 69% porosity. The Fe25Mn scaffolds had the ε-martensite and γ-austenite phases, while the Fe30Mn and Fe35Mn scaffolds had only the γ-austenite phase. All iron-manganese alloys exhibited weakly paramagnetic behavior, confirming their potential to be used as MRI-friendly bone substitutes. The *in vitro* biodegradation rates of the scaffolds were very much enhanced (*i.e.*, 4.0 to 4.6 times higher than that of porous iron), with the Fe35Mn alloy exhibiting the highest rate of biodegradation (*i.e.*, 0.23 mm/y). While the elastic moduli and yield strengths of the scaffolds decreased over 28 days of *in vitro* biodegradation, those values remained in the range of cancellous bone. The culture of preosteoblasts on the porous iron-manganese scaffolds revealed that cells could develop filopodia on the scaffolds, but their viability was reduced by the effect of biodegradation. Altogether, this research marks a major breakthrough and demonstrates the great prospects of multi-material extrusion-based 3D printing to further address the remaining issues of porous iron-based materials and, eventually, develop ideal bone substitutes.

Statement of significance

3D printed porous iron biomaterials for bone substitution still encounter limitations, such as the slow biodegradation and magnetic resonance imaging incompatibility. Aiming to solve the two fundamental issues of iron, we present *ex-situ* alloyed porous iron-manganese scaffolds fabricated by means of multi-material extrusion-based 3D printing. Our porous iron-manganese possessed enhanced biodegradability, non-ferromagnetic property, and bone-mimicking mechanical property throughout the *in vitro* biodegradation period. The results demonstrated a great prospect of multi-material extrusion-based 3D printing to further address the remaining challenges of porous iron-based biomaterials to be an ideal biodegradable bone substitutes.

© 2021 The Author(s). Published by Elsevier Ltd on behalf of Acta Materialia Inc.
This is an open access article under the CC BY license (http://creativecommons.org/licenses/by/4.0/)

1. Introduction

The treatment of large bone defects requires interventions aimed at bringing the healthy bone back [1]. Current clinical

* Corresponding author.
E-mail address: n.e.putra@tudelft.nl (N.E. Putra).

https://doi.org/10.1016/j.actbio.2021.07.042
1742-7061/© 2021 The Author(s). Published by Elsevier Ltd on behalf of Acta Materialia Inc. This is an open access article under the CC BY license (http://creativecommons.org/licenses/by/4.0/)

strategies, *i.e.*, autografts, allografts and xenografts, impose major limitations on the treatment, including insufficient supply and the risk of foreign body rejection and infection [2]. As an alternative strategy, synthetic biomaterials have been developed to act as bone substitutes and assist in the restoration of bone defects. Until today, different types of porous biomaterials, based on polymers, ceramics, and metals have been developed [3–5]. The earlier developments were mostly focused on bio-inert materials, mimicking the mechanical properties of bone tissue and aiming to achieve osseointegration [6,7]. The inert nature of these biomaterials, however, does not allow complete bone regeneration, as they remain permanently at the implantation site. The latest generation of bone substitutes has been designed to be biodegradable and bioactive for facilitating and encouraging bone ingrowth [8,9]. Within this class of biomaterials, biodegradable metals, such as iron and its alloys, possess higher strengths than magnesium-, zinc-, polymer- and ceramic-based biodegradable materials and, therefore, offer exciting prospects for application as load-bearing bone substitutes [10–12].

Iron is one of the promising biodegradable metals. Unlike magnesium, it has excellent processability [13,14] and its rate of biodegradation is slow enough to provide continued mechanical support while the bone regeneration process progresses. However, the *in vivo* biodegradability of iron is so low that it may elicit immunogenic responses similar to bio-inert materials [15]. In addition, iron is ferromagnetic by nature, which complicates the imaging procedure for the patients who are exposed to a strong magnetic field, typically in magnetic resonance imaging (MRI) [16]. To address both fundamental issues of iron, alloying of iron with manganese has been proposed [17]. The addition of 28 wt% or more manganese to iron promotes austenicity, making the alloy anti-ferromagnetic and, thus, MRI-friendly [18]. Furthermore, manganese has a lower standard electrode potential than iron (*i.e.*, -1.18 V versus -0.44 V). Because iron and manganese form solid solution, the standard electrode potential of the alloy tends to decrease with increasing manganese content, thus allowing for faster biodegradation [19]. As for the biocompatibility, despite naturally occurring in the human body, iron and manganese at high doses can be toxic [20,21]. Considering all these factors is of great importance in the design of iron-manganese alloys intended for bone substitution.

For bone substitution, the geometrical design of Fe-Mn alloy scaffolds needs to imitate the hierarchical structure of native bone as well as its mechanical properties. A rationally designed and precisely manufactured porous structure is one of the key geometrical features [22,23]. The porosity, pore shape, and pore sizes will not only influence the mechanical properties, but also determine (to a large extent) the biodegradation kinetics and biofunctionality of the resulting biomaterial [12,24–27]. In realizing complex geometrical designs, iron-manganese alloys have been fabricated with a variety of techniques, such as casting [28–30], powder metallurgy [31–33], space holder method [24–26,34], and sponge impregnation [35]. However, these techniques are restricted to achieving non-conforming porous structures without precisely controlled pore characteristics and limited pore interconnectivity. Recent advances in 3D printing technologies have removed the restrictions and presented an unprecedented opportunity to fabricate geometrically ordered bone-substituting materials of almost any structural design [12,36].

In the recent years, porous iron-manganese alloy structures have been 3D printed with binder jetting [37,38] and selective laser melting [39–41]. As compared to those techniques, extrusion-based 3D printing followed by debinding and sintering offers a more robust and versatile approach to the *ex situ* alloying of Fe and Mn and the fabrication of porous multi-material scaffolds that are otherwise highly demanding for the other 3D printing techniques [42–44]. To date, no study on extrusion-based 3D printed porous iron-manganese scaffolds has appeared in the literature. Here, we report, for the first time, the successful fabrication of *ex situ*-alloyed porous iron with 25, 30, or 35 wt% manganese using extrusion-based 3D printing. We also performed comprehensive characterization of the porous materials, including *in vitro* biodegradation behavior, electrochemical responses, and biodegradation-dependent mechanical properties, as well as *in vitro* cytocompatibility assessment using the MC3T3-E1 cell line.

2. Materials and methods

2.1. Powder mixture and ink preparation

Iron powder (99.88 wt% purity; spherical morphology; particle size distribution: D_{10} = 25.85 µm, D_{50} = 39.93 µm and D_{90} = 53.73 µm, Fig. 1**a**) and manganese powder (99.86 wt% purity; irregular morphology; particle size distribution: D_{10} = 7.69 µm, D_{50} = 20.89 µm and D_{90} = 41.58 µm, Fig. 1**b**) were used as the starting materials for the preparation of iron-manganese-containing inks. Both powders were purchased from Material Technology Innovations Co. Ltd., China. Iron-manganese powder mixtures (with 25, 30, and 35 wt% manganese, hereafter denoted as Fe25Mn, Fe30Mn, and Fe35Mn, respectively) were prepared using a roller mixer (CAT Zipperer GmbH, Germany) at 80 rpm for 18 h. As for the binder preparation, hydroxypropyl methylcellulose (hypromellose) powder (M_w ~86 kDa, Sigma Aldrich, Germany) was dissolved in a water-ethanol solution with a 5 wt% concentration [45]. The addition of ethanol to the solvent was intended to minimize the reactivity of the binder with the manganese powder. Then, the mixed iron-manganese powders were blended with the hypromellose binder to prepare 3D printable iron-manganese-containing inks at a mass ratio of 7:1 [45]. The mixed powder mass ratios in the inks corresponded to the volume ratios of 49.6% for Fe25Mn, 49.7% for Fe30Mn, and 49.8% for Fe35Mn. The ink density was calculated from the volume fractions of the iron-manganese powder and the binder and their theoretical densities. In addition, the rheological behaviors of the inks were studied using an MCR302 rheometer (Anton Paar GmbH, Germany).

2.2. Extrusion-based 3D printing, debinding and sintering

Porous iron-manganese scaffolds (10 mm in diameter and 10.5 mm in height) were designed as a lay-down pattern with the following characteristics: strut size = 410 µm; strut spacing = 400 µm; layer thickness = 328 µm; relative porosity = 50%; surface area = 40.4 cm^2 (Fig. 1**c**). The iron-manganese-containing inks were extruded using a 3D BioScaffolder 3.2 printer (GeSiM Bioinstruments, Germany) at a printing speed of 3.5 mm/s and under pressures of 280 kPa, 290 kPa, and 300 kPa for the Fe25Mn, Fe30Mn, and Fe35Mn inks, respectively, through a tapered nozzle tip (nozzle size = 410 µm), in a printing pattern of 0 ° and 90 ° that switched every other layer (Fig. 1**c**). Thereafter, the as-printed iron-manganese scaffolds were dried for at least 30 min and were placed inside a tube furnace (STF16/180, Carbolite Gero Ltd., UK) under highly pure argon flow (purity = 99.9999%; inlet pressure = 1 bar). Debinding and sintering were respectively performed at 350 °C for 3 h and at 1200 °C for 6 h followed by natural cooling in the furnace. The as-sintered porous iron-manganese scaffolds were ultrasonically cleaned in isopropyl alcohol for 15 min prior to subsequent investigations. The exact compositions of the porous iron-manganese alloys after sintering were determined by using an inductively coupled plasma optical emission spectroscope (ICP-OES, iCAP 6500 Duo, Thermo Scientific, USA).

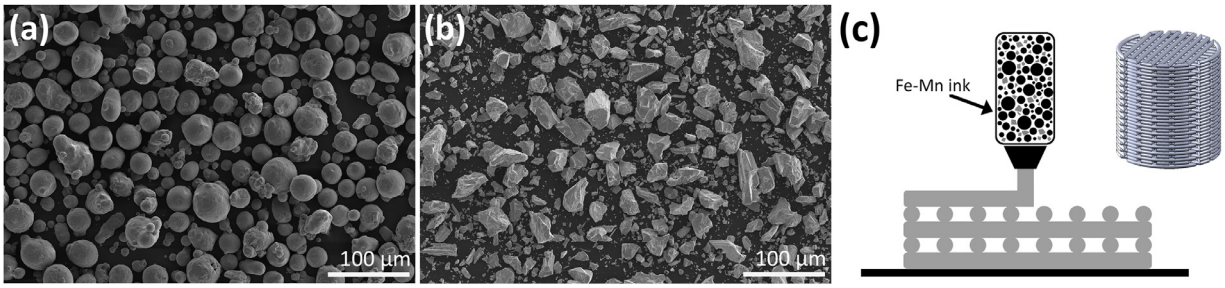


Fig. 1. Morphologies of (a) iron and (b) manganese powders, and (c) a schematic illustration of extrusion-based 3D printing and the design of porous iron-manganese scaffolds in a lay-down pattern of 0 ° and 90 °.

2.3. Macro-and microstructural characterization

The dimensions of the porous iron-manganese alloy scaffolds were measured to determine the dimensional changes occurring during sintering. The porous structures of the iron-manganese alloy scaffolds were observed using a scanning electron microscope (SEM, JEOL JSM-IT100, Japan) and their morphological characteristics (*i.e.*, strut width and strut spacing) were determined. The absolute porosities were calculated based on the dry weighing method:

$$\varphi_p = \left(1 - \frac{m_p/\rho_{ink}}{V_{bulk}}\right) \times 100\% \quad (1)$$

$$\varphi_s = \left(1 - \frac{m_s/\rho_{Fe-Mn}}{V_{bulk}}\right) \times 100\% \quad (2)$$

where φ_p and φ_s are, respectively, the absolute porosities of the as-printed and the as-sintered iron-manganese scaffold [%], m_p and m_s are the masses of the as-printed or as-sintered iron-manganese scaffold [g], respectively, V_{bulk} is the bulk volume [cm^3], ρ_{ink} is the density of the iron-manganese-containing ink (*i.e.*, 4.36 g/cm^3 for Fe25Mn, 4.35 g/cm^3 for Fe30Mn, and 4.34 g/cm^3 for Fe35Mn), and $\rho_{Fe\text{-}Mn}$ is the theoretical density of the iron-manganese alloy (*i.e.*, 7.70 g/cm^3 for Fe25Mn, 7.66 g/cm^3 for Fe30Mn, and 7.63 g/cm^3 for Fe35Mn).

In addition, the interconnectivity of the pores of the iron-manganese alloy scaffolds was determined using the Archimedes' principle and according to the ASTM standard B963-13 [46]:

$$\varphi_i = \left(\frac{\rho_e}{\rho_o} \times \frac{m_{ao} - m_a}{m_{ao} - m_{eo}}\right) \times 100\% \quad (3)$$

where φ_i is the interconnected porosity [%], ρ_e is the density of ethanol (*i.e.*, 0.789 g/cm^3), ρ_o is the density of oil (*i.e.*, 0.919 g/cm^3), m_a is the mass of the iron-manganese alloy scaffold weighed in air [g], and m_{ao} and m_{eo} are the masses of the oil-impregnated iron-manganese alloy scaffolds weighed in air and in ethanol [g], respectively.

In addition, the cross sections of the as-sintered porous iron-manganese alloy struts were observed using SEM and the elemental compositions were mapped using X-ray energy dispersive spectroscopy (EDS, JEOL JSM-IT100, Japan). The regions of interest on the cross sections of struts were defined and the pore area was selected using ImageJ (NIH, USA). The solid fraction of strut (X) was calculated as:

$$X = \left(1 - \frac{Pore\ area}{Total\ area\ of\ ROI}\right) \times 100\% \quad (4)$$

2.4. Phase identification

The phases in the porous iron-manganese alloys were identified using an X-ray diffractometer (XRD, D8 Advance, Bruker, USA) equipped with a graphite monochromator and a Lynxeye position-sensitive detector. The diffractometer was operated in the Bragg-Brentano geometry using Co Kα radiation, at 45 kV and 40 mA, at a step size of 0.030 °, and a counting time of 2 s per step. The resulting XRD patterns were analyzed with Diffrac Suite.EVA v5.2 software.

2.5. In vitro *immersion tests and biodegradation product characterization*

In vitro immersion tests were performed using a revised simulated body fluid (r-SBF) [47] under the following condition: a static fluid environment; pH = 7.40; immersion for 1, 2, 7, 14 and 28 d; temperature = 37 ± 0.5 °C; relative humidity (RH) = 95%; CO_2 = 5%; in an ambient O_2 atmosphere; 6.7 mL medium per 1 cm^2 scaffold surface area [48]. We chose r-SBF as the biodegradation medium, because its nominal ion concentrations are exactly the same as those of the total blood plasma [47]. All porous iron-manganese specimens (in triplicate for every time point) were sterilized at 120 °C for 2 h prior to the immersion tests and the medium was filtered through a 0.22 µm pore size (Merck Millipore, Germany). The pH values of the medium were recorded using a pH electrode (InLab Expert Pro-ISM, METTLER TOLEDO, Switzerland). To determine the mass loss, the *in vitro* biodegradation products on the porous iron-manganese alloy specimens were dissolved in 6 M hydrochloric acid with addition of 3.5 g/L hexamethylene tetramine at room temperature during a period of 10 min, followed by ultrasonic cleaning in isopropyl alcohol for 15 min. Then, the samples were dried, and the mass loss values were measured. The cleaning cycle was repeated and the mass loss was plotted against the number of cleaning cycles to obtain the most accurate value, according to the ASTM standard G1-03 [49]. The remaining iron-manganese material was weighed using a balance with an accuracy of 0.1 mg. The average corrosion rate was determined using the mass loss values and according to the ASTM standard G31-72 [50]:

$$CR_{immersion}\ [mm/year] = 8.76 \times 10^4 \times \frac{m}{A \times t \times \rho} \quad (5)$$

where m is the mass loss [g], A is the surface area of the porous iron-manganese specimen [cm^2] calculated based on the initial scaffold design value, t is the time span of *in vitro* immersion [h], and ρ is the theoretical density of the iron-manganese alloy (g/cm^3).

Following uninterrupted immersion until the selected time points (*i.e.*, 1, 2, 7, 14, and 28 d), the morphological characteristics of the biodegradation products on the periphery and in the center of the porous iron-manganese alloys were observed using SEM (JEOL JSM-IT100, Japan) and the chemical elements in the biodegradation product compounds were identified using EDS (JEOL JSM-IT100, Japan). The solid fraction of the remaining iron-manganese material after uninterrupted immersion for 28 d was

calculated using ImageJ (NIH, USA) and Eq. (4). The phases of the biodegradation products after 28 d immersion were analyzed using XRD (D8 Advance, Bruker, USA). Furthermore, the soluble iron, manganese, calcium, and phosphate ion concentrations in r-SBF were measured using ICP-OES (iCAP 6500 Duo, Thermo Scientific, USA).

2.7. Magnetic susceptibility evaluation

Porous iron-manganese specimens (with an average mass of 39.7 ± 4 mg, in triplicate, before and after *in vitro* immersion for 28 d) were exposed to an applied magnetic field of 2 T at room temperature in a vibrating sample magnetometer chamber (VSM 7307, Lake Shore, USA). Porous Ti-6Al-4V samples were added to the tests as the control group. The magnetic hysteresis loops obtained were analyzed to determine the saturation magnetization, remanence magnetization, and magnetic susceptibility values.

2.8. Electrochemical measurements

The electrochemical responses of the porous iron-manganese alloys were investigated using a three-electrode setup connected to a Bio-Logic SP-200 potentiostat (Bio-Logic Science Instruments, France). The electrochemical system consisted of a Ag/AgCl electrode as the reference electrode, a graphite rod as the counter electrode, and the iron-manganese alloy specimen as the working electrode. The specimens were prepared through partial embedding in a thermoplastic acrylic resin followed by ultrasonic cleaning in isopropyl alcohol and thorough drying. Subsequently, the specimens were immersed in the r-SBF medium (temperature = 37 ± 0.5 °C; pH = 7.40). The exposed surface area of the specimens was calculated based on the initial design value of the scaffold. Before the electrochemical analysis, the system was stabilized for 1 h to obtain a steady open circuit potential (OCP). The linear polarization resistance (LPR) and electrochemical impedance spectroscopy (EIS) tests were performed in triplicate at different time points up to 28 d of immersion. Porous iron specimens were included as a control group in the LPR measurements. The LPR tests were conducted at a scan rate of 0.167 mV/s from -25 to + 25 mV *vs.* OCP while the EIS tests were carried out over a frequency range of 100 kHz to 10 mHz using a sine amplitude of 10 mV *vs.* OCP.

2.9. Uniaxial compression tests

The compressive mechanical properties of the porous iron-manganese specimens, including the specimens retracted at the selected time points of the *in vitro* immersion test, were evaluated using a mechanical testing machine (Zwick Z100, Germany) with a 100 kN load cell. The tests were displacement-controlled and were performed using a crosshead speed of 3 mm/min, in triplicate, according to the ISO standard 13314:2011 [51]. The slope of the initial linear line in the stress-strain curve was taken as the quasi-elastic gradient (hereafter, referred to as the elastic modulus). A 0.2% offset line, parallel to the initial linear region, was drawn and the intersection with the curve was taken as the yield strength. The plastic deformation curves up to a strain of 0.1 mm/mm were fitted to Eq. (6) to quantify the initial strain-hardening exponent degree of the porous iron-manganese specimens.

$$\sigma = K\varepsilon^{n} \tag{6}$$

where σ is stress [MPa], K is the strength coefficient, ε is strain [mm/mm], and n is the strain-hardening exponent.

2.10. Cytocompatibility evaluation

2.10.1. Cell culture and preparation of iron-manganese alloy extracts

Mouse preosteoblast cells (MC3T3-E1, Sigma Aldrich, Germany) were pre-cultured for 7 d in a cell incubator under the following conditions:37 ± 0.5 °C, 95% RH, and 5% CO_2. The cell culture medium was made of α-minimum essential medium (α-MEM,) without ascorbic acid, but supplemented with 10% fetal bovine serum (FBS) and 1% penicillin/streptomycin (p/s). All the cell culture medium components were purchased from Thermo Fisher Scientific, USA.

Extracts were obtained after 72 h incubation of sterilized porous iron-manganese specimens (10.15 mm in diameter and 10.55 mm in height) in the cell culture medium [52]. The extracts were prepared at a sample-to-medium ratio of 5 cm^2/mL (100%) and were further diluted to 75, 50, and 25% from the initial concentration. The surface area calculation was based on the initial design value. Prior to use, the extracts were filtered through a 0.22 µm pore size (Merck Millipore, Germany) and were stored at 4 °C. In addition, the concentrations of iron and manganese ions in the 100% extract were measured using ICP-OES (iCAP 6500 Duo, Thermo Scientific, USA).

2.10.2. Indirect assays: Presto Blue assay and F-actin/nucleus staining

The metabolic activity of preosteoblasts cultured in the iron-manganese alloy extracts was evaluated using the PrestoBlue assay (Thermo Fisher Scientific, USA) as described in our previous publication [45]. The preosteoblasts (1×10^4 cells) were cultured with 200 µL iron-manganese alloy extracts in 48-well plates (in triplicate). As for the negative control groups, the cells were cultured in the normal cell culture medium. After 1, 3, and 7 d of cell culture, the PrestoBlue reagent (Thermo Fisher Scientific, USA) was added to the cells and the absorbance values were quantified using a Victor X3 microplate reader (PerkinElmer, the Netherlands) at a wavelength of 530–590 nm. The cellular metabolic activity was calculated as:

$$Metabolic\ activity\ [\%] = \frac{Absorbance\ (specimen)}{Absorbance\ (negative\ control)} \times 100 \tag{7}$$

The F-actin and nucleus of the preosteoblasts, after being exposed to the iron-manganese alloy extracts for 3 d, were stained using rhodamine phalloidin (Thermo Fisher Scientific, USA) and 4′,6-diamidino-2-phenylindole (DAPI, Life Technologies, USA), following the procedure reported in our previous publication [45]. Subsequently, the morphology of the *F*-actins and nuclei was observed using a fluorescence microscope (ZOE cell imager, Bio-Rad, USA).

2.10.3. Direct assays: viable cell count and live/dead staining

The MC3T3-E1 preosteoblasts (5×10^4 cells per sample) were seeded into the porous iron-manganese specimens (1.3 mm in height and 10.15 mm in diameter) and were cultured for 1, 4, 7, 14, and 28 d in 6-well plates containing 8 mL of the cell culture medium. Porous pure iron specimens were included as the control group. After cell culture, preosteoblasts were detached from the specimens and the viable cells were counted using the Trypan blue assay (Bio-Rad, USA) with an automated cell counter (TC20, Bio-Rad, USA) as described in our previous publication [45]. Furthermore, the morphology of the preosteoblasts after 4 d of culture with the porous iron-manganese specimens was observed using calcein and ethidium homodimer-1 staining (Thermo Fisher Scientific, USA) and SEM imaging. In addition, the porous iron-manganese specimens immersed in the cell culture medium (in the incubator) for 7 and 28 d were investigated to observe the

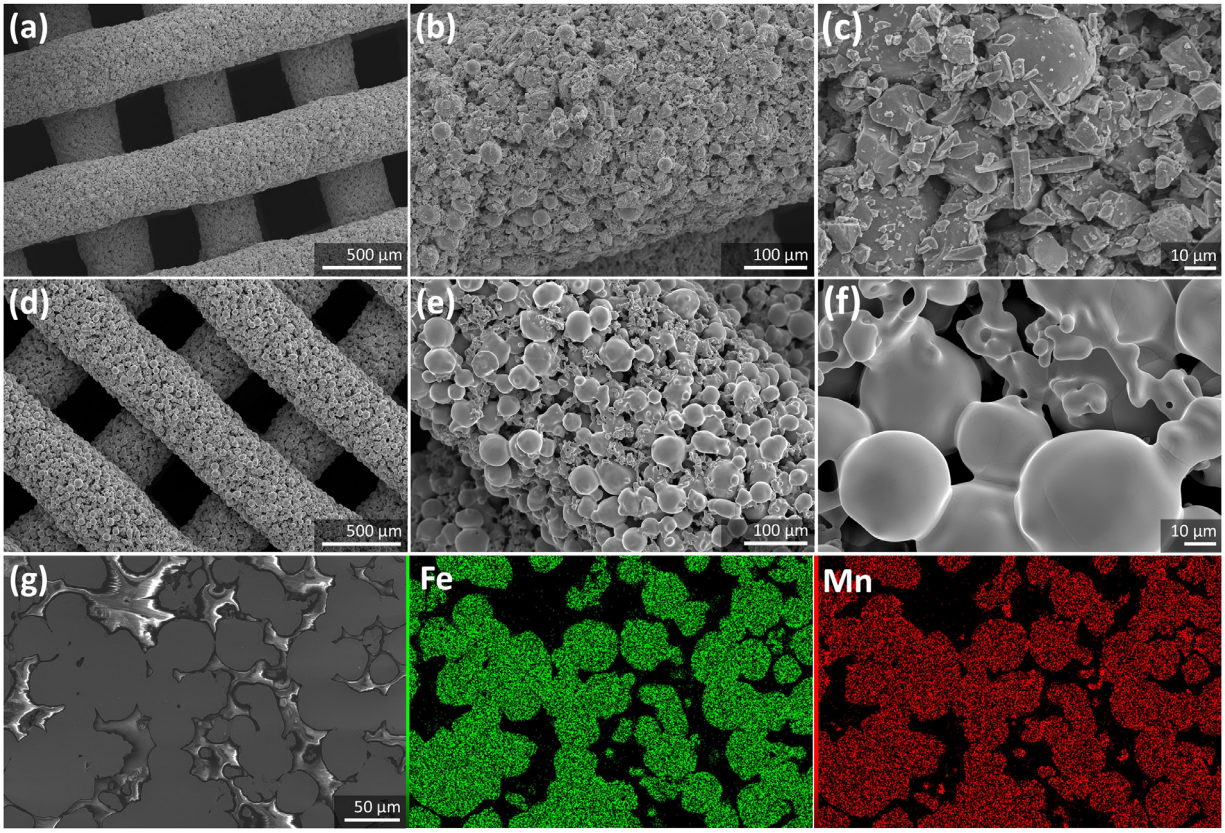


Fig. 2. Morphologies of porous Fe35Mn: (a, b, c) in the as-printed condition and (d, e, f) in the as-sintered condition at different magnifications, and (g) EDS mapping on the cross-section of porous iron-manganese struts. (For interpretation of the references to color in this figure, the reader is referred to the web version of this article.)

strut morphology and identify the biodegradation products that could have affected the cytocompatibility.

2.11. Statistical analysis

The statistical analysis of the PrestoBlue and viable cell count results was performed with two-way ANOVA, followed by a Tukey multiple comparison *post hoc* test ($^{****} = p < 0.0001$, $^{***} = p < 0.001$, $^{**} = p < 0.01$, and $^{*} = p < 0.05$, *n.s.* = not significant).

3. Results

3.1. Characteristics of the porous iron-manganese alloys

The extrusion-based 3D printed porous iron-manganese scaffolds, *i.e.*, Fe35Mn (Fig. 2), Fe30Mn (**Fig. S1**), and Fe25Mn (**Fig. S2**) exhibited very similar geometric characteristics to the original scaffold design of the 0 ° and 90 ° pattern (Fig. 2**a**). The optimum mixed powder loading and the shear-thinning behavior of the iron-manganese-containing ink (**Fig. S3**) allowed a smooth 3D printing process to create the scaffolds with a high aspect ratio and free-standing feature. Furthermore, iron and manganese particles from the elemental powders were homogenously distributed in the struts (Fig. 2**a–c**).

After sintering, the porous iron-manganese alloy scaffolds (Figs. 2**d, S1, S2**) slightly expanded in size (*i.e.*, a 0.3 to 0.5% increase in diameter and a 1.4 to 1.6% increase in height). On the periphery, spherical powder particles fused and were occasionally bridged by irregularly shaped powder particles (Figs. 2**e–f, S1, S2**). The specific configuration of powder particle bonding resulted in micro-porosity inside the struts, with solid fractions equal to 67 ± 2%, 64 ± 3%, and 63 ± 2% for the Fe25Mn, Fe30Mn, and Fe35Mn scaffolds, respectively. From the cross-sectional EDS analyze, manganese completely diffused into the iron matrix (Figs. 2**g, S1, S2**), confirming the occurrence of alloying during the sintering process and the successful synthesis of the materials.

The as-sintered iron-manganese alloys had an average absolute porosity of 69% and a pore interconnectivity up to 98.6%. The detailed structural characteristics of the as-printed and as-sintered porous iron-manganese scaffolds are presented in Table 1. As a result of the complete diffusion of manganese into iron (Fig. 2**g**), the porous Fe25Mn alloy had the dual ε-martensite and γ-austenite phases, whereas the porous Fe30Mn and Fe35Mn alloys had only the γ-austenite phase (Fig. 3**a**). In addition, a very small amount (< 2 wt%) of manganese oxide was detected in the scaffolds, which was actually present in the initial manganese powder before ink preparation. The chemical compositions of the as-sintered porous iron-manganese alloys slightly deviated from the design values (Table 2).

3.2. Magnetic properties

In the applied magnetic field of 2 T, all the porous iron-manganese alloys exhibited very low saturation magnetization values (*i.e.*, 0.35 Am^2/kg for Fe25Mn, 0.32 Am^2/kg for Fe30Mn, and Fe35Mn), which were quite close to the magnetization value of Ti-6Al-4V (Fig. 4). After 28 d of immersion in r-SBF, the magnetization increased up to 0.58 Am^2/kg, but the values were still at a relatively low level. The slight increase in magnetization could be due to the ferrimagnetic behavior of the residual biodegradation products (*e.g.*, iron or manganese oxides) that remained on the struts even after the ultrasonic cleaning step. Furthermore, the magnetic susceptibility of all the porous iron-manganese alloys did not sig-

Table 1
Structural characteristics of the extrusion-based 3D printed porous iron-manganese scaffolds.

Sample groups		Strut width (μm)	Strut spacing (μm)	Absolute porosity (%)	Interconnected porosity (%)
Fe25Mn	**As-printed**	410 ± 6	400 ± 6	43 ± 5	-
	As-sintered	411 ± 6	398 ± 6	69 ± 2	67 ± 1
Fe30Mn	**As-printed**	409 ± 5	401 ± 5	44 ± 4	-
	As-sintered	412 ± 7	398 ± 7	69 ± 2	67 ± 1
Fe35Mn	**As-printed**	409 ± 5	402 ± 6	43 ± 2	-
	As-sintered	412 ± 6	398 ± 5	69 ± 1	68 ± 1

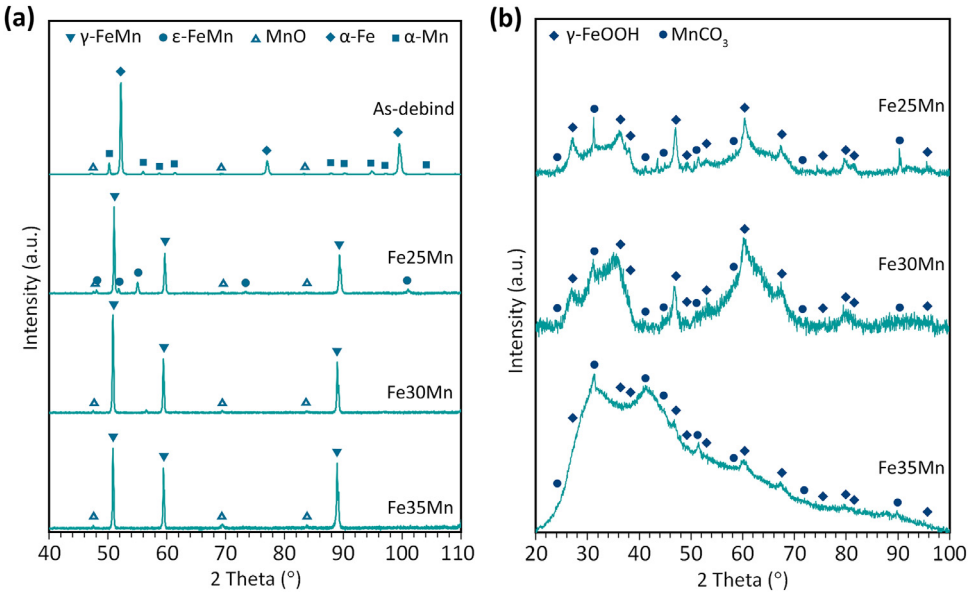


Fig. 3. Phase compositions of (a) the porous iron-manganese scaffolds in the as-debinded and as-sintered conditions and (b) after 28 d of *in vitro* biodegradation.

t

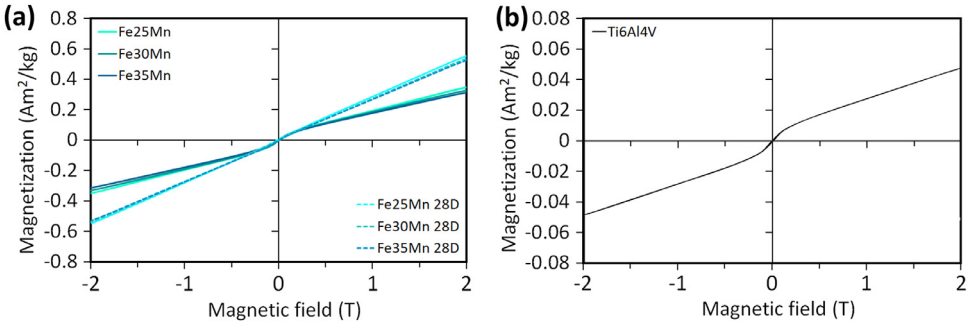


Fig. 4. Magnetization curves of (a) the porous iron-manganese alloys (as-built and after 28 d of *in vitro* biodegradation) and (b) porous Ti-6Al-4V.

Table 2
Chemical compositions of the as-sintered porous iron-manganese alloys.

As-sintered sample	Fe (wt%)	Mn (wt%)	Impurities
Fe25Mn	74.94 ± 0.14	24.87 ± 0.16	0.19 ± 0.02
Fe30Mn	70.05 ± 0.05	29.72 ± 0.02	0.23 ± 0.03
Fe35Mn	65.31 ± 0.11	34.51 ± 0.07	0.18 ± 0.06

nificantly change (χ = 3.0–4.4 × 10^{-3}) even after 28 d of immersion.

3.3. In vitro *biodegradation performance*

During the static *in vitro* immersion tests, yellow-brownish corrosion products were deposited on the porous iron-manganese alloy strut surfaces (Fig. 5**a**). The immersion tests in a cell incubator provided a precisely controlled 5% CO_2 atmosphere. The pH level of the r-SBF medium was maintained between 7.61–7.63 throughout the 28 d of the immersion test (Fig. 5**b**). The average mass loss due to biodegradation was larger for the alloy with a higher manganese content (Fig. 5**c**). At the beginning of the immersion test, (*i.e.*, after 1 d), the *in vitro* biodegradation rates of the porous iron-manganese specimens were 3.37 ± 0.19 mm/y, 3.76 ± 0.16 mm/y, and 4.53 ± 0.28 mm/y for Fe25Mn, Fe30Mn, and Fe35Mn, respectively (Fig. 5**d**). After 28 d of immersion, however, the biodegradation rates decreased to 0.18 mm/y, 0.20 mm/y, and 0.23 mm/y (± 0.01), respectively (Fig. 5**d**).

During *in vitro* biodegradation, iron and manganese ions were gradually released to the r-SBF medium (Fig. 5**e,f**). The ion release reached a peak after 14 d of immersion, and then decreased. The iron ion concentrations were relatively low from the all scaffold groups (*i.e.*, approximately 1 ppm at 14 d) (Fig, 5**e**). Meanwhile,

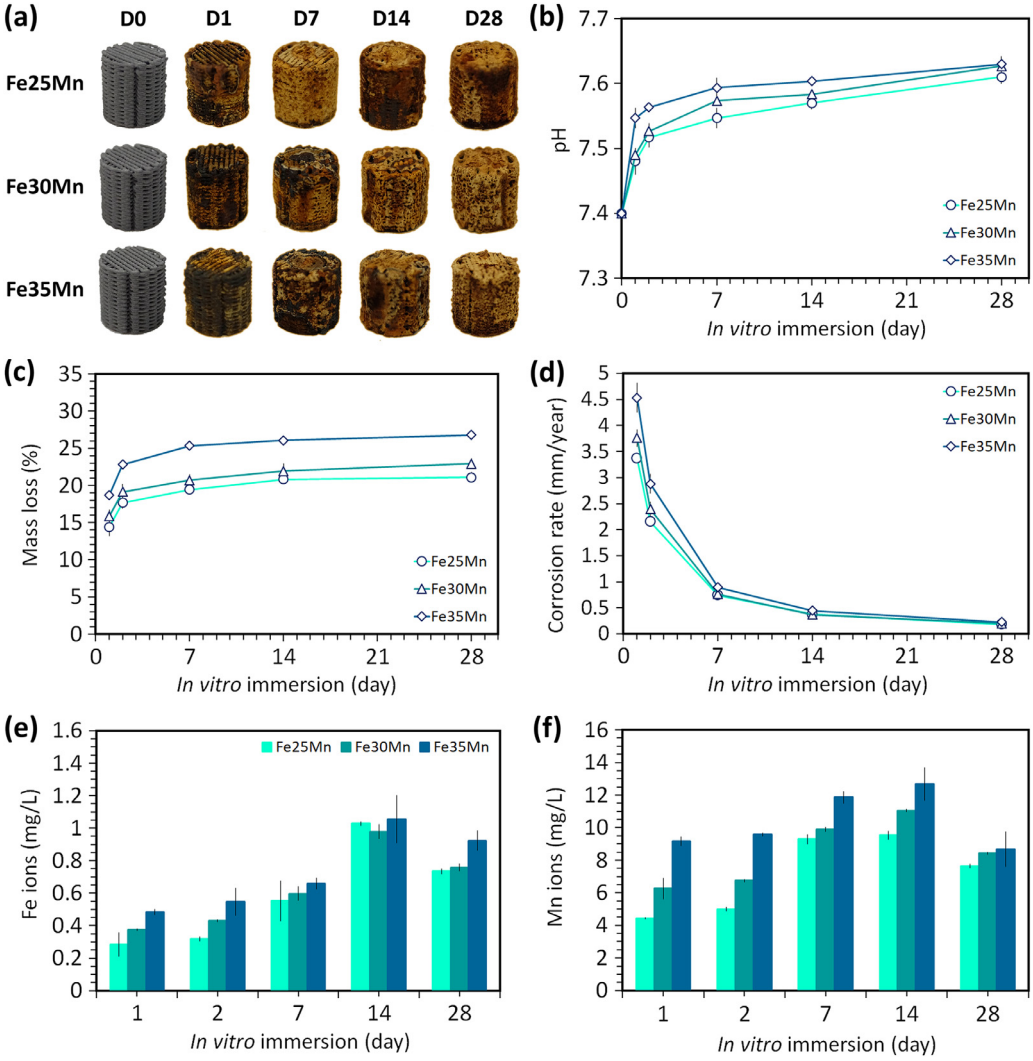


Fig. 5. *In vitro* biodegradation characteristics of the porous iron-manganese alloys: (a) visual inspection of the scaffolds at different time points of biodegradation, (b) variations of pH values of the immersion medium with time, (c) mass losses with time, (d) corrosion rates with time, and the concentrations of (e) iron and (f) manganese ions released during biodegradation. (For interpretation of the references to color in this figure, the reader is referred to the web version of this article.)

the manganese ion concentrations reached 9.5–12.7 ppm at the same time point (Fig. 5**f**). The amount of manganese ion release from the alloy with a higher manganese content was larger. As the biodegradation continued to day 28, the base material (*i.e.*, the iron-manganese alloy) was progressively consumed, accompanied by the decreases in the solid fraction to 42 ± 8% (Fe25Mn), 39 ± 3% (Fe30Mn), and 31 ± 9% (Fe35Mn).

3.4. Characteristics of the biodegradation products

A dense layer of biodegradation products was formed on the struts after 24 h of immersion (Fig. 6**a**). The biodegradation products grew with time and almost filled the macropores of the scaffolds at day 28 (Fig. 6**b–d**). Similar observations were made for the porous Fe30Mn (**Fig. S4**) and Fe25Mn (**Fig. S5**) scaffolds. In addition, the peripheral biodegradation products were identified to be iron oxyhydroxide (γ-FeOOH) and rhodochrosite ($MnCO_3$) (Fig. 3**b**). Correspondingly, the major elements present in the peripheral biodegradation products were found to be iron, manganese, oxygen, and carbon (Fig. 6**e–j**).

After 24 h immersion, the biodegradation products at the periphery of the porous Fe35Mn scaffolds transformed from a mixture of iron- and manganese-based compounds (Fig. 6**e, h**) to those with a higher concentration of manganese at day 7 (Fig. 6**f, i**), and finally changed to iron-based compounds at day 28 (Fig. 6**g, j**). During the 28 d of immersion, the biodegradation products at the periphery of the Fe30Mn scaffold specimens (**Fig. S4**) evolved in a similar manner to those on the porous Fe35Mn scaffold specimens. However, the biodegradation products on the periphery of the Fe25Mn scaffold specimens were predominantly made of iron-based compounds after 24 h of immersion. Afterwards, the compounds transformed to manganese-based compounds after 7 d and back to iron-based compounds after 28 d (**Fig. S5**). At the center of the scaffolds with pore networks, the 28 d biodegradation products were predominantly carbon- and oxygen-based compounds (Figs. 6**k, S4,5**).

3.5. Electrochemical measurements

The OCP values of the porous iron-manganese alloys were stable during the 28 d of biodegradation (Fig. 7**a**). After 24 h of immersion, the OCP values were -757 ± 2 mV, -745 ± 3 mV, and -761 ± 6 mV for Fe25Mn, Fe30Mn, and Fe35Mn, respectively. After 28 d of immersion, the OCP values only changed marginally to -746 ± 4 mV, -745 ± 3 mV, and -737 ± 3 mV, respectively. On the other hand, the OCP values of porous iron increased from -

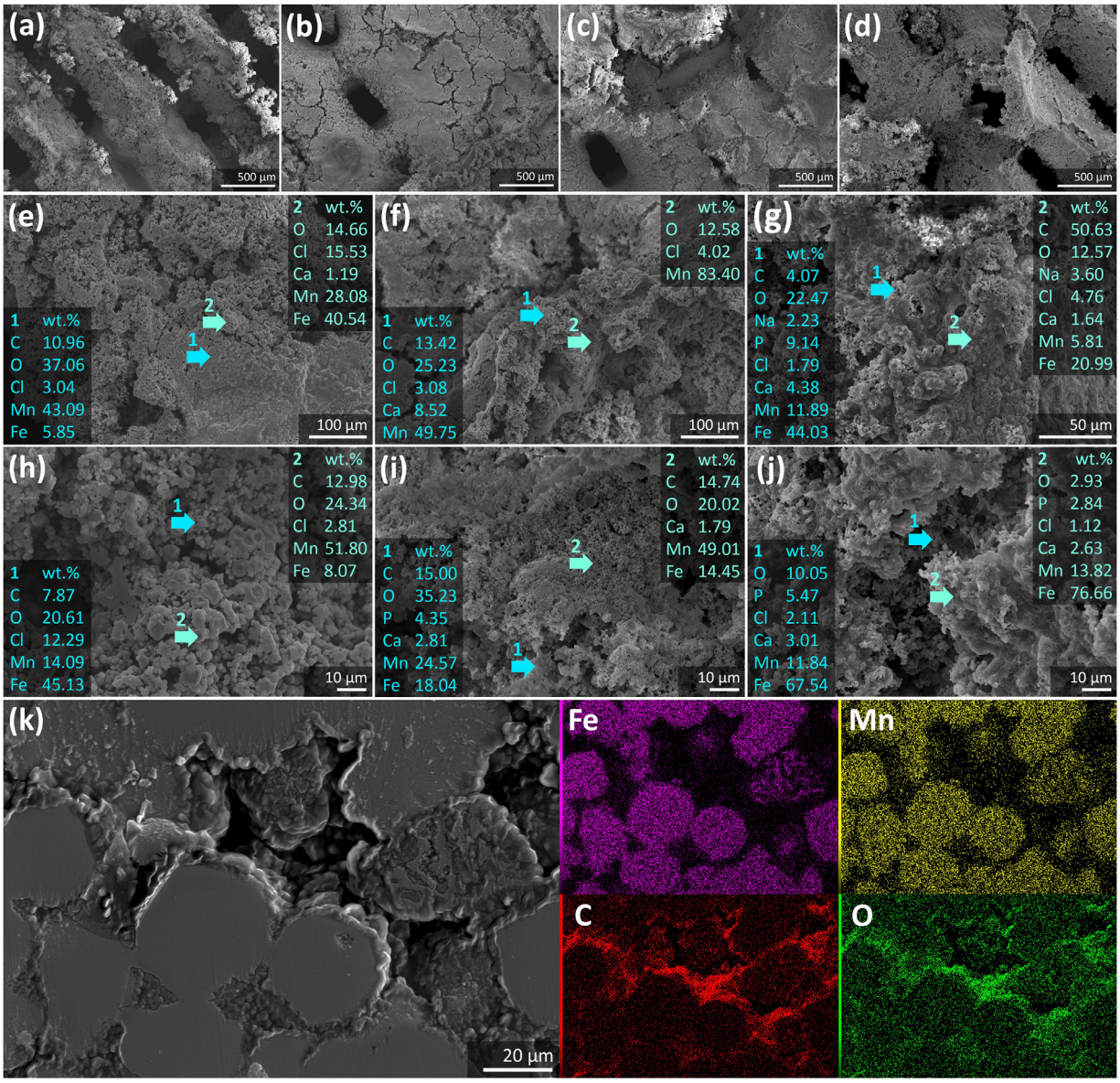


Fig. 6. Morphologies and chemical compositions of the *in vitro* biodegradation products on porous Fe35Mn struts: on the periphery after (a, e, h) 24 h, (b, f, i) 7 d, (c) 14 d, and (d, g, j) 28 d of biodegradation, and (k) at the center of the scaffolds after 28 d of biodegradation. The arrow and number indicate the location of EDS analysis. (For interpretation of the references to color in this figure, the reader is referred to the web version of this article.)

706 ± 2 mV after 24 h of immersion to -608 ± 49 mV after 28 d of immersion. From the LPR measurements, the average polarization resistance values of the porous iron-manganese alloys showed an increasing trend during the initial 14 d of immersion and remained relatively stable afterwards (Fig. 7**b**). Meanwhile, the average polarization resistance values of porous iron increased with immersion time. After 24 h, the average polarization resistance values were 1.9 ± 0.3 kΩ.cm^2, 1.9 ± 0.2 kΩ.cm^2, 3.5 ± 0.6 kΩ.cm^2 for Fe25Mn, Fe30Mn, and Fe35Mn, respectively. After 28 d of immersion, the average polarization resistance values increased to 3.3 ± 0.6 kΩ.cm^2, 5.1 ± 1.3 kΩ.cm^2, and 4.8 ± 1.5 kΩ.cm^2, respectively. For the porous iron scaffolds, the average polarization resistance values significantly increased from 3.2 ± 0.8 kΩ.cm^2 after 24 h of immersion to 23.4 ± 4.4 kΩ.cm^2 after 28 d of immersion (Fig. 7**b**).

The impedance Nyquist plots of the porous iron-manganese alloys displayed semicircles that grew larger with increasing immersion time up to 14 days and slightly fluctuated towards 28 d of immersion (Fig. 7**c**). At the low frequency (*i.e.*, 0.01 Hz), the Bode impedance magnitude values of the porous iron manganese alloys had a similar trend as the polarization resistance (Fig. 7**d**). After 24 h, the impedance magnitude values at 0.01 Hz were 2.5 ± 0.9 kΩ.cm^2, 2.0 ± 0.2 kΩ.cm^2, 3.9 ± 0.7 kΩ.cm^2 for Fe25Mn, Fe30Mn, and Fe35Mn, respectively. After 28 d of immersion, the values increased to 4.3 ± 1.5 kΩ.cm^2, 4.5 ± 1.1 kΩ.cm^2, and 4.8 ± 1.4 kΩ.cm^2, respectively.

3.6. Mechanical properties

Under uniaxial compression, all the porous iron-manganese specimens exhibited smooth stress-strain curves that started with a linear elastic region, followed by a plastic deformation region that corresponded to the typical strain-hardening behavior (Fig. 8**a**). Among all the as-sintered iron-manganese alloys, the porous Fe25Mn alloy exhibited the highest strain-hardening rate with a strain-hardening exponent of 0.80 (Fig. 8**a**). Meanwhile, the porous Fe30Mn and Fe35Mn specimens demonstrated strain-

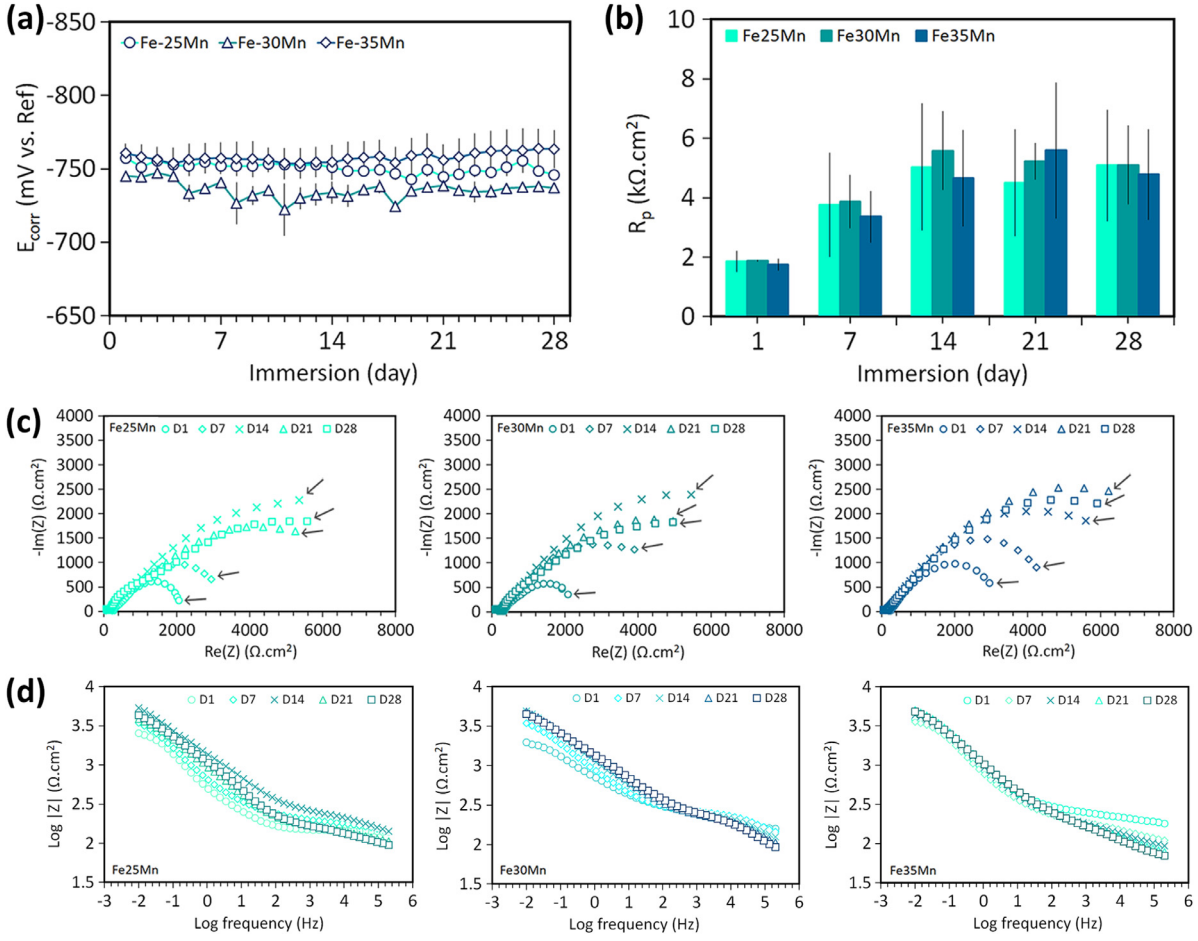


Fig. 7. Electrochemical responses of the porous iron-manganese alloys during 28 d of biodegradation: (a) OCP and (b) polarization resistance values from the LPR measurements; (c) impedance Nyquist and (d) Bode plots at different time points.

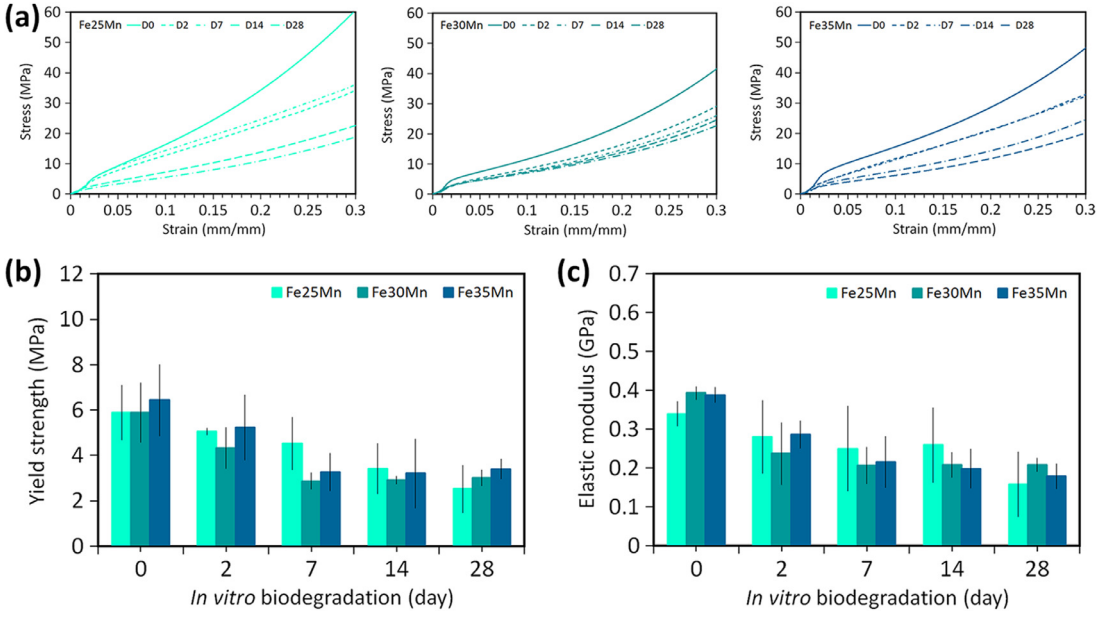


Fig. 8. Compressive mechanical properties of the porous iron-manganese alloys: (a) the stress-strain curves, (b) the yield strength and (c) elastic modulus values during 28 d of biodegradation.

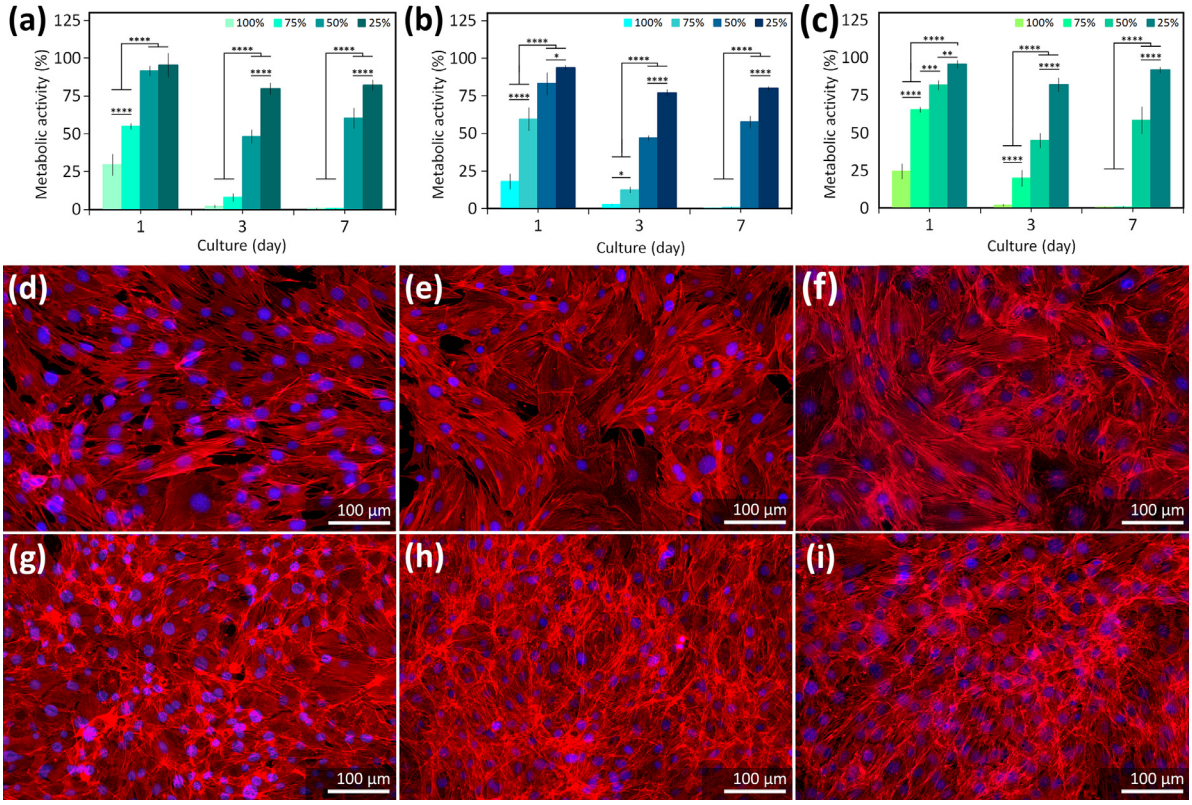


Fig. 9. Indirect cytocompatibility of the various porous iron-manganese alloys for MC3T3-E1 preosteoblasts: (a, b, c) the metabolic activity of preosteoblasts after 1, 3, and 7 d of culture; rhodamine phalloidin (red) and DAPI (blue) fluorescence staining of preosteoblasts after 3 d of culture in (d, e, f) the 75% and (g, h, i) the 50% extracts of Fe25Mn, Fe30Mn and Fe35Mn, respectively. **** = $p < 0.0001$, *** = $p < 0.001$, ** = $p < 0.01$, and * = $p < 0.05$. (For interpretation of the references to color in this figure legend, the reader is referred to the web version of this article.)

hardening exponent values of 0.74 and 0.66, respectively. Prior to the *in vitro* immersion tests, the porous iron-manganese specimens (Fe25Mn, Fe30Mn, and Fe35Mn) possessed yield strengths of 5.9 ± 1.2 MPa, 5.9 ± 1.3 MPa, and 6.4 ± 1.6 MPa, respectively. The elastic modulus values were 0.34 ± 0.03 GPa, 0.39 ± 0.02 GPa, 0.39 ± 0.02 GPa, respectively. As a result of biodegradation, the yield strengths (Fig. 8**b**) and elastic moduli (Fig. 8**c**) of all the scaffold groups gradually decreased over time. After 28 d, the yield strengths were 3.0 ± 1.0 MPa, 3.0 ± 0.3 MPa, and 3.4 ± 0.4 MPa for Fe25Mn, Fe30Mn, and Fe35Mn, respectively. At the same time, the elastic modulus values decreased to 0.16 ± 0.08 GPa, 0.21 ± 0.02 GPa, and 0.18 ± 0.03 GPa, respectively. Furthermore, the strain-hardening exponent declined up to 0.57 after 28 d of biodegradation.

3.7. In vitro *cytotoxicity against preosteoblasts*

The extracts of the porous iron-manganese specimens contained iron and manganese ions with concentrations of 60.2 ± 1.1 mg/mL and 52.4 ± 0.9 mg/mL for Fe25Mn, 62.2 ± 1.1 mg/mL and 46.7 ± 0.5 mg/mL for Fe30Mn, and 62.8 ± 1.7 mg/mL and 37.5 ± 0.8 mg/mL for Fe35Mn, respectively. The indirect cell tests (*i.e.*, the PrestoBlue assay) (Fig. 9**a–c**) revealed immediate cytotoxicity for all the 100% iron-manganese extracts with less than 30% metabolic activity of preosteoblasts after 24 h of cell culture and almost no metabolic activity after 7 d of cell culture. Similar cytotoxic effects were observed for all the 75% iron-manganese alloy extracts after 3 d of the culture and onwards. For the 50% iron-manganese alloy extracts, the metabolic activity of the cells reduced during the initial 3 d of cell culture and recovered after 7 d of cell culture. However, the values were still around 60%. Nonetheless, the preosteoblasts could proliferate and spread nicely forming a confluent cell layer after 3 d of cell culture in the 75% extracts (Fig. 9**d–f**) and 50% extracts (Fig. 9**g–i**). The 25% iron-manganese extracts behaved the best with a more than 85% metabolic activity of preosteoblasts at all the time points.

The direct culture of the preosteoblasts on the porous iron-manganese alloys resulted in a decreased number of viable cells after 24 h of culture relative to the pure iron scaffolds (*i.e.*, 1.4–1.8 × 10^4 cells) (Fig. 10**a**). The number of preosteoblasts depleted after 7 d of culture to 0.9–1.3 × 10^5 cells and fluctuated during the subsequent cell culture period (*i.e.*, 1.3–1.5 × 10^4 cells and 1.3–1.4 × 10^4 cells after 14 and 28 d, respectively). The preosteoblasts attached to the surfaces developed many filopodia, although the cellular body was rather round-shaped (Fig. 10**b**). Furthermore, a few green fluorescence-stained (viable) preosteoblasts were observed on all the porous iron-manganese specimens (Fig. 10**c–e**). Nonetheless, the fluorescent staining showed uniformly seeded cells on the struts, indicating the high seeding efficiency of the assays.

4. Discussion

The extrusion-based 3D printed porous iron-manganese scaffolds developed in this research exhibited a highly encouraging potential to meet most of the requirements for iron-based bone substitution, including (i) weak paramagnetic properties with a very low magnetic susceptibility, meaning that the synthesized materials successfully tackled the fundamental issue of the MRI-incompatibility of pure iron, and (ii) significantly enhanced *in vitro* biodegradability (*i.e.*, 0.20–0.23 mm/y) due to the addition of 30–35 wt% manganese to iron. The achieved values fall into the range of the suitable biodegradation rates for ideal bone substitutes (*i.e.*,

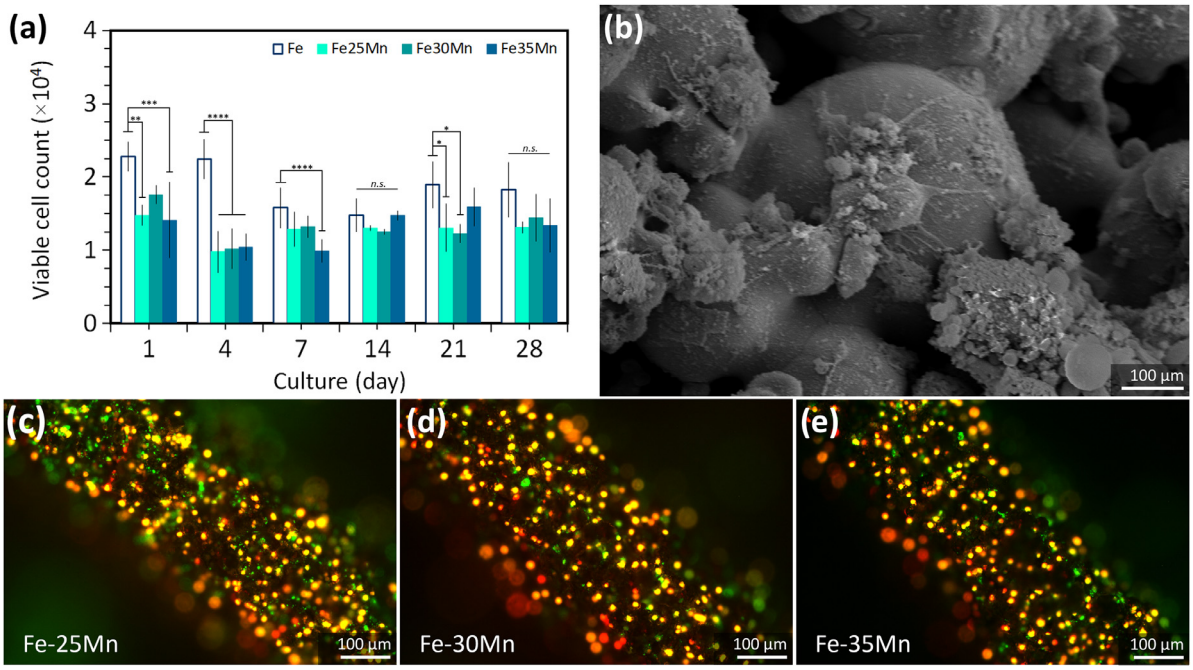


Fig. 10. Direct cytocompatibility of the porous iron-manganese alloys: (a) the number of viable MC3T3-E1 preosteoblasts after up to 28 d of culture; (b) the morphology of preosteoblasts after 4 d of culture on the porous iron-manganese specimens; (c, d, e) calcein acetoxymethyl (green, showing viable cells) and ethidium homodimer-1 (red, showing damaged cells) fluorescence staining of preosteoblasts after 4 d of culture on porous Fe25Mn, Fe30Mn, and Fe35Mn, respectively. **** = $p < 0.0001$, *** = $p < 0.001$, ** = $p < 0.01$, * = $p < 0.05$, and *n.s.* = not significant. (For interpretation of the references to color in this figure legend, the reader is referred to the web version of this article.)

0.2–0.5 mm/y) [53]. Furthermore, the porous alloys possessed sufficient mechanical properties even after a 28 d biodegradation period (*i.e.*, E = 0.16–0.21 GPa and σ_y = 3.0–3.4 MPa), and these values stayed within the range of the cancellous bone [54]. These results can be considered major breakthroughs in the development of porous iron-based biodegradable implants, motivating the follow-up research to address the important issue of cytocompatibility.

4.1. Extrusion-based 3D printing of the porous iron-manganese scaffolds

In the present research, extrusion-based 3D printing was successfully applied for the multi-material additive manufacturing of *ex situ*-alloyed porous iron-manganese scaffolds. The key to a successful fabrication process lies in a proper iron-manganese-containing ink formulation that should be stable and possess the required rheological properties for extrusion-based 3D printing. The hypromellose binder in the ink provides the ink with shear-thinning properties (**Fig. S3**), which is particularly important for stable flow of the ink during the 3D printing process. The mixed iron-manganese powder loadings of 49.55 vol% (Fe25Mn), 49.66 vol% (Fe30Mn), and 49.78 vol% (Fe35Mn) resulted in printable iron-manganese inks with the ability to retain the strut shape upon extrusion. The ink formulations and 3D printing process parameters delivered the porous iron-manganese scaffolds with structural characteristics that were close to the original design (Fig. 2**a–c**).

The 3D printed porous iron-manganese scaffolds were subjected to debinding to remove the binder in the inks at the temperature where the binder decomposed [45]. Considering more compact morphologies of the as-printed iron-manganese alloy struts, the debinding time was extended to 3 h from 1 h that was previously used for pure iron [45], to allow thorough binder removal and prevent any interactions between the binder residual and iron-manganese powder mixture. Thereafter, the porous iron-manganese scaffolds were sintered to facilitate the diffusion of manganese into iron and simultaneously get the powder particles bonded (Fig. 2**d–g**). At high temperatures, manganese tends to be volatile [55]. As the temperature increases for the sintering stage, manganese sublimates and the vapor flows into the micropores of the struts, settling on the surface of the iron powder particles. Then, manganese diffuses into iron powder particles, leading to the expansion of the original iron particles, and the creation of a solid solution. As a consequence of this process, the as-sintered porous iron-manganese scaffolds expanded by 1.6%, which was also encountered in other fabrication routes involving sintering [32].

Iron-manganese alloys with more than 23 wt% manganese have a minor amount of the ε-martensite phase, together with the γ-austenite phase [56]. When higher than 28 wt% manganese is added to iron, only the γ-austenite single phase is present [56]. In the present research, the ε-martensite and γ-austenite dual phases were detected in the porous Fe25Mn alloy and only the γ-austenite single phase was found in the porous Fe30Mn and Fe35Mn alloys (Fig. 3**a**), which is in agreement with the literature. The presence of these phases instead of the α-ferrite phase is of crucial importance, as they provide anti-ferromagnetic behavior [57,58], which is required for iron-based biomaterials to be MRI-friendly.

Furthermore, the as-sintered porous iron-manganese alloys possessed a relatively low solid fraction of 63–67%, which may be a result of the diffusion of 25–35 wt% manganese into iron, leaving open pore spaces within the struts [33]. All the iron-manganese alloy scaffolds had an absolute porosity of 69% and up to 98.6% of pores were interconnected (Table 1). For bone substitution applications, open pores are advantageous for both biodegradability and biological properties. Well-channeled pore networks offer large surface area between powder particles, hence encouraging biodegradation and stimulating bone cell adhesion and ingrowth [59,60].

Table 3
Magnetic properties of the extrusion-based 3D-printed porous iron-manganese alloys in comparison with those found in the literature.

Sample groups		Magnetic susceptibility		Saturation magnetization at 2 T (Am^2/kg)	Remanence magnetization (Am^2/kg)	Ref.
		χ ($\times 10^{-3}$)	χ_g ($\times 10^{-6}$, m^3/kg)			
Fe		5100 ± 47	640 ± 6	190.4 ± 0.1	0.0656 ± 0.0008	This study
Fe25Mn	**D0**	3.5 ± 0.2	0.44 ± 0.03	0.349 ± 0.003	0.0004 ± 0.0003	
	D28	4.4 ± 1.1	0.57 ± 0.14	0.58 ± 0.02	0.0006 ± 0.0003	
Fe30Mn	**D0**	3.4 ± 0.3	0.44 ± 0.04	0.32 ± 0.01	0.0006 ± 0.0003	
	D28	3.0 ± 0.1	0.39 ± 0.02	0.54 ± 0.04	0.0006 ± 0.0002	
Fe35Mn	**D0**	3.3 ± 0.1	0.42 ± 0.02	0.316 ± 0.003	0.0004 ± 0.0003	
	D28	3.1 ± 0.2	0.40 ± 0.03	0.53 ± 0.02	0.0006 ± 0.0003	
Ti6Al4V		0.35 ± 0.04	0.08 ± 0.01	0.045 ± 0.001	0.0022 ± 0.0002	
Fe25Mn		-	0.19	0.08*	0.011	[61]
Fe30Mn		-	0.19	0.08*	0.005	
Fe35Mn		-	0.18	0.07*	0.003	
Fe30Mn6Si1Pd		-	-	0.4	-	[30]
Porous Fe30Mn6Si1Pd		-	-	13.5	-	[25]
Fe35Mn		-	-	0.5***	-	[33]

* at 0.5 T magnetic field; **expressed in A/m; *** at 5 T.

4.2. Magnetic behavior of the porous iron-manganese alloys

The ε-martensite and γ-austenite phases in the iron-manganese alloys are known for their anti-ferromagnetic properties [61]. In the present research, the magnetization of the porous iron-manganese alloys was measured in a high magnetic field of 2 T, which is the typical intensity used in clinical MRI machines [62]. The magnetization saturation values of the porous iron-manganese alloys were three orders of magnitude lower than that of pure iron (Table 3), even after 28 d of biodegradation with the formation of degradation products that were ferrimagnetic. The magnetic properties of the porous iron-manganese alloys in comparison with the values found in the literature are listed in Table 3.

Even when the applied magnetic field is removed, the remanent magnetization of pure iron is still relatively high (*i.e.*, 0.0656), compared to that of the iron-manganese alloys (*i.e.*, < 0.0007) or Ti-6Al-4V (*i.e.*, 0.0022). The magnetic susceptibility values (χ) of the porous iron-manganese alloys (*i.e.*, 3.0–4.4 $\times 10^{-3}$) were three orders of magnitude lower than that of pure iron (*i.e.*, 5.1). However, the values were still one order of magnitude higher than that of Ti-6Al-4V (*i.e.*, 0.3 $\times 10^{-3}$). A material whose magnetic susceptibility value falls into the range of $10^{-5} < |\chi - \chi_{water}| < 10^{-2}$ (with $\chi_{water} = -9.05 \times 10^{-6}$) belongs to the first kind of magnetic field compatible materials [63]. The magnetic properties of such a material do not interfere significantly with the magnetic field of MRI machines, but may produce MRI artefacts [63]. Based on this theoretical analysis, the porous iron-manganese alloys developed in the present research can be categorized as the magnetic field compatibility of the first kind, which is in the same category as Ti-6Al-4V.

For most weakly paramagnetic medical devices (*e.g.*, titanium-based implants), MRI artefacts are inevitably observed, although the material is considered to be MRI-safe [64]. During MRI, a sharp transition in the magnetic susceptibility occurs between the paramagnetic material and the human tissue (*e.g.*, soft tissue = -9.05 $\times 10^{-6}$ and cortical bone = -8.86 $\times 10^{-6}$ [63]), which affects the readout [65]. It has recently been reported that a reduction in the volume of MRI artefacts can be achieved by introducing a porous geometry into the material [66–68], which is relevant to the bone substitution application. In general, our results have shown the prospects of iron-manganese scaffolds as weakly paramagnetic iron-based bone substitutes. In the near future, the detailed tests of the porous iron-manganese alloys, including the evaluation of the magnetically induced torque and displacement force, and radiofrequency-induced heating [62], will be performed to better understand the paramagnetic behavior of these biomaterials.

4.3. *Biodegradation* in vitro

The *in vitro* biodegradation rates of the porous iron-manganese alloys at 28 d (*i.e.*, 0.18, 0.20, and 0.23 mm/year for Fe25Mn, Fe30Mn, and Fe35Mn, respectively) are in the range of the values reported for Fe-Mn alloys in the literature (Table 4). Assuming a stable biodegradation rate beyond the 28 d of the immersion tests, the porous Fe30Mn and Fe35Mn alloys degraded at the rates that are within the range of the ideal biodegradation rates suggested for bone substitutes (*i.e.*, 0.2–0.5 mm/year) [53]. The values were about 4.0 to 4.6 times higher than that of porous pure iron, fabricated by using the same 3D printing technique [45]. An addition of manganese to iron is known to improve the rate of biodegradation significantly by lowering the standard electrode potential [19,33]. In addition, the manganese-rich regions in the struts (Fig. 2**g**) may promote local micro-galvanic corrosion. Besides the porous struts with original powder particle boundaries, the diffusion of manganese into iron powder particles created more open micropores, as compared to the pure iron counterpart [45], which would significantly increase the available surface area in the struts for the initiation of biodegradation.

The biodegradation reactions can be described in a simplified way as:

$$\text{Anodic reaction :} \quad Fe \rightarrow Fe^{2+} + 2e^- \tag{8}$$

$$Mn \rightarrow Mn^{2+} + 2e^- \tag{9}$$

$$\text{Cathodic reaction :} \quad 2H_2O + O_2 + 4e^- \rightarrow 4OH^- \tag{10}$$

As the biodegradation progresses Eqs. (8),(9), the local solution become alkaline due to the OH^- products of the cathodic reaction Eq. (10). The alkalinity of the solution with raised local pH will induce the precipitation of Fe- and Mn-based biodegradation products. For example, Fe^{2+} can be hydrolyzed to form $Fe(OH)_2$ Eq. (11). Then, $Fe(OH)_2$ can be further oxidized to form $Fe(OH)_3$ Eq. (12). Since $Fe(OH)_3$ is less stable, it will transform into a more stable compound (*e.g.*, FeOOH, Eq. (12)):

$$Fe^{2+} + 2H_2O \rightarrow Fe(OH)_2 + 2H^+ \tag{11}$$

$$4Fe(OH)_2 + O_2 + 2H_2O \rightarrow 4Fe(OH)_3 \rightarrow 4FeOOH + 4H_2O \tag{12}$$

Table 4
In vitro biodegradation rates obtained from the immersion tests of the extrusion-based 3D-printed porous iron-manganese alloys in comparison with those found in the literature.

Materials and fabrication method		Porosity (%)	Immersion condition	Time point	Corrosion rate (mm/year)	Ref.
Fe25Mn **Fe30Mn** **Fe35Mn**	**Extrusion-based 3D printing and sintering**	69	Static, 37 °C, 5% CO_2, r-SBF	28 d	0.18-0.23	This study
Fe35Mn	**Space holder**	27.3 ± 0.6 40.0 ± 3.9 48.2 ± 0.3	Static, 37 °C, SBF	14 d	0.5	[24]
Fe35Mn	**Binder jetting**	39.3 ± 1.5	Static, 37 °C, Hank's balanced salt solution	28 d	0.03	[38]
Fe30Mn	**Space holder**	43	Static - 37 °C, 5% CO_2, DMEM	30 d	0.79	[26]
Fe20Mn	**Powder metallurgy and sintering**	13.9	Quasi static - 37 °C, 5% CO_2, Hank's balanced salt solution	30 d	0.116 ± 0.009	[33]
Fe30Mn		20.6			0.141 ± 0.012	
Fe35Mn		21.3			0.306 ± 0.022	
Fe30Mn	**Space holder**	32.5 ± 3	Static, 37 °C, 5% CO_2, αMEM	30 d	0.389 ± 0.05	[34]
Fe25Mn	**Selective laser melting**	66.72 ± 2.4	Static, 37 °C, SBF	30 d	0.23 ± 0.05	[39]
Fe35Mn	**Selective laser melting**	42.6 ± 0.2	Quasi static, 37°C, SBF	30 d	0.42 ± 0.03	[40]
Fe30Mn	**Sponge impregnation and sintering**	84.6 ± 2.9	Static - 37 °C, SBF	14 d	0.81	[35]

Besides FeOOH, the precipitated biodegradation products may contain calcium-based, phosphate-based, or carbonate-based compounds as well through the following reactions Eqs. (13)–(15):

$$3Fe^{2+} + 2PO_4^{3-} + 8H_2O \rightarrow Fe_3(PO_4)_2 \cdot 8H_2O \downarrow \quad (13)$$

$$5Ca^{2+} + 3PO_4^{3-} + 2OH^- \rightarrow Ca_5(PO_4)_3 \cdot (OH)_2 \downarrow \quad (14)$$

$$Fe^{2+}/Mn^{2+}/Ca^{2+} + HCO_3^- \rightarrow FeCO_3/MnCO_3/CaCO_3 \downarrow + H^+ + e^- \quad (15)$$

From these potential precipitation reactions, only γ-FeOOH and $MnCO_3$ were detected (Fig. 3**b**). The calcium and phosphorus precipitates of low concentrations were identified only at the periphery, mostly during the late periods of the biodegradation tests (Fig. 6**f,g**).

As a whole, the biodegradation products formed on the struts on the periphery as well as at the center of the scaffold (Fig. 6), thereby passivating the base material and decreasing the biodegradation rate during the subsequent immersion period (Fig. 5**d**). The gradual densification of the morphology of the corrosion products (Fig. 6) slows down the corrosion process too. During biodegradation, the variations of iron and manganese ion release with time could be attributed to their participation in the corrosion products (Fig. 5**e, f**). Manganese ions were released ~10 times more than iron ions throughout the 28 d biodegradation, which is in agreement with the data reported in other studies [69,70]. The faster release of manganese ions is closely related to the medium composition and atmospheric condition. It has been reported that bicarbonate ions (HCO_3^-) promote faster manganese ion release [70]. In addition, biodegradation, occurring under a 5% CO_2 atmosphere, helps in maintaining the availability of HCO_3^- in the r-SBF medium [71]. These interactions not only induce manganese ion release but also cause the formation of carbonate compounds (*i.e.*, $MnCO_3$, Eq. (15)).

As for the iron-based biodegradation products, the formation of γ-FeOOH was identified (Fig. 3**b**). Unlike the porous pure iron [45], iron phosphate biodegradation product did not form during the biodegradation of the porous iron-manganese alloys, as observed by other researchers [33,61]. In addition, calcium phosphate precipitation did not seem to have happened to a great extent. The concentrations of calcium and phosphorus elements detected at the periphery were relatively low (Fig. 6**i,j**). In the center of the scaffolds (**Fig. S6**), only very small amounts of calcium were detected in the Fe30Mn and Fe35Mn scaffolds along with iron, manganese, carbon and oxygen. Although the local solution could be alkalinized by the cathodic response during the early period of the immersion tests Eq. (10), the pH value would be balanced by the hydrogen ions released during the hydrolysis of ferrous ions Eq. (11) and the precipitation of $MnCO_3$ compounds Eq. (15). A recent study showed that the local pH value of porous iron-manganese remained between 7.1 to 7.3 after 24 h immersion in Hank's balanced salt solution [72,73]. In this case, the formation of stable calcium phosphate might have been impeded, since the precipitation was more favorable at a higher pH value [74]. Moreover, the absence of calcium phosphate compounds might be possible due to the swift release of iron or manganese ions and the formation of iron-manganese products during biocorrosion [25].

Overall, the biodegradation products of the porous iron-manganese alloys, both at the periphery and at the center of the scaffolds, appeared to be more chemically diverse (Fig. 6) than those of porous pure iron [45]. After 28 d of immersion, a variety of elements, including calcium, phosphorus, sodium, carbon, oxygen, and even traces of chlorine, were present in the peripheral degradation products of the porous iron-manganese alloys (Fig. 6**g, j**). At the center, carbon was detected to be participating in the oxide-containing degradation products (Fig. 6**k**).

The electrochemical responses of the porous iron-manganese alloys indicated stable OCP values throughout the immersion period, as compared to porous iron scaffolds (Fig. 7**a**). In addition, the polarization resistance values of the porous iron-manganese alloys are much lower, compared to the polarization resistance exhibited by porous iron (Fig. 7**b**). Such trends of OCP and polarization resistance imply that iron-manganese biodegradation products are less passivating, compared to those for pure iron. This means that the porous iron-manganese alloys can maintain the same level of propensity to biodegrade over the immersion time. Moreover, both Nyquist (Fig. 7**c**) and Bode impedance plots (Fig. 7**d**) demonstrated the same trend as the LPR results. The Nyquist plots of porous iron-manganese remain in a semicircle shape throughout the immersion time (Fig. 7**c**), unlike the impedance plots of porous iron scaffolds reported in our previous publication [45]. Altogether, the EDS analyze (Fig. 6) and electrochemical results (Fig. 7) demonstrated that the biodegradation products, particularly those involving the participation of manganese, influence the corrosion resistance of the iron-based passivating layer. Although a more detailed study would be required, this finding is in agreement with the hypothesis suggested by other researchers on iron-manganese alloys containing more than 20 wt% manganese [33,75,76].

Furthermore, the volume losses of the porous iron-manganese alloys found in the immersion tests were 21.1–26.8% (calculated from the mass loss values) after 28 d. Although the corrosion rates of the porous iron-manganese alloys are in the range of the values reported in the literature (Table 4), the recent *in vivo* research on a porous Fe30Mn biomaterial (with 38–47% porosity) has reported 10.1–20.9% volume loss after 48 weeks of implantation [41]. The biodegradation of iron-based biomaterials has been reported to be slower *in vivo* than *in vitro* [77]. This is because the biodegradation of iron-manganese is strongly dependent on the dissolved O_2 availability Eq. (10). The *in vitro* immersion tests in the current research were performed in an ambient O_2 atmosphere (*i.e.*, 21%), which was very different from the low concentration of dissolved O_2 near bone marrow region (*e.g.*, < 4.2%) [78]. Therefore, future *in vitro* biodegradation tests of iron-based materials should be performed in a controlled O_2 environment. More *in vivo* studies on the porous iron-manganese alloys need to be carried out to determine to what extent the *in vitro* biodegradation results can be translated to the actual conditions.

4.4. Mechanical behavior

Biodegradation decreases the mechanical properties of bone substitutes over time. The rate of bone regeneration and the rate of decrease in the mechanical properties of the implant should, therefore, be balanced with each other to ensure that the mechanical support continues to be available at all times. The porous iron-manganese biomaterials presented here exhibited bone-mimicking mechanical properties in the range of cancellous bone (E = 0.02–2.0 GPa and σ_y = 0.1–30 MPa [54]) even after 28 d of *in vitro* biodegradation. The influence of the manganese content on the mechanical properties of our porous biomaterials was limited, which is in contrast with the observations made for bulk iron-manganese alloys that show decreases in the yield strength as the manganese content increases [61]. This could be explained, considering the strong dependence of the mechanical properties of the porous materials on the bonding between the sintered powder particles and the distribution of the random open micropores present in the struts. In addition, the γ-austenite phase in the porous iron-manganese could retain the ductility of the materials even after biodegradation (Fig. 8**a**), which is an important mechanical property for bone substitutes to be able to endure cyclic loading.

Due to the decreases in the solid fraction of the iron-manganese scaffolds after 28 d of biodegradation, the yield strengths and elastic moduli of the porous iron-manganese alloys declined by 47.2–57.1% and 47.1–53.9%, respectively (Fig. 8**b, c**). Degradation of the mechanical properties has also been reported in other studies after *in vitro* biodegradation [40,79]. In *in vivo* studies, however, reductions in elastic modulus (by as much as 42.3%) and yield strength (by 23.3%) have been reported only after 48 weeks [41]. Although the retrieved specimens may still contain newly matured bone tissue in the pores of the scaffolds, which may contribute to its mechanical properties, the higher mechanical properties that are observed *in vivo* are most likely due to the slower biodegradation of the materials *in vivo*, as previously discussed.

4.5. Cytocompatibility

The biocompatibility of an iron-manganese alloy is closely related to the concentration of iron and manganese ions released into the cell culture medium. To evaluate the indirect cytotoxicity of the porous iron-manganese alloys, the iron-manganese extracts were prepared under an extreme conditions (*i.e.,* 72 h extraction in the physiological conditions [80]). The metabolic activity of preosteoblasts (Fig. 9**a–c**) improved with the dilution ratio of the extract. The original 100% iron-manganese extracts showed instantaneous metabolic inhibition for preosteoblasts and cell lysis with no viable cells left for actin and nucleus staining. For this reason, all the 100% iron-manganese extracts would be categorized as cytotoxic grade 4, according to ISO 10993-5 [80]. Likewise, the 75% iron-manganese extracts demonstrated an immediate metabolic activity reduction, however, a nice spreading and a healthy morphology of the cells were still present (Fig. 9**d–f**). Therefore, the 75% extracts fall into the (moderately) cytotoxic grade 3 category. After 2 × dilution (50%), the iron-manganese extracts were categorized as mildly toxic (grade 2), where less than 50% metabolic inhibition was observable, although the growth of preosteoblasts did not appear to be hindered (Fig. 9**g–i**). At 4 × dilution (25%), the iron-manganese alloy extracts exhibited a non-cytotoxic response (grade 1) with > 80% preosteoblast metabolic activity.

The inhibitory concentrations (IC_{50}) of iron and manganese ions towards preosteoblasts have been reported to be 53.2–88.5 mg/L and 4.8 mg/L, respectively [20]. In the 100% iron-manganese extracts, the iron ion release was 60.2–62.8 mg/L, which is in the range of the IC_{50} value. At the same time, the manganese ion release, which varied between 37.5–52.4 mg/L, is significantly higher than the IC_{50} value, which is why the extracts at higher concentrations were cytotoxic. The systemic toxicity due to iron ions is usually rare, because most iron ions are not free-flowing, but chaperoned by proteins (*e.g.*, transferrin [81]). However, extensive exposure of free iron ions can induce oxidative stresses [82]. In the case of manganese, bone is one of the tissues with a significant manganese reserve [83]. This could explain the observation that despite the high concentration of manganese ions even after 4 × dilution, the preosteoblast metabolic activity remained undisturbed. Nevertheless, a too high manganese ion concentration in bone is strongly related to neurotoxicity [83].

The present direct cultures involved a high ratio of cell culture medium volume to the sample surface area, which may better mimic the actual human body conditions, considering the possibility that more medium could help reduce the local accumulation of metal ions. Our results, however, demonstrated the cytotoxicity during the initial period of cell culture, *i.e.*, during 4 d, and cell growth inhibition up to 28 d (Fig. 10**a**). The cytotoxic results were similar to those obtained in several *in vitro* studies [25,34], but at the same time contradicted those of other studies [35,39,41,84]. To understand the direct cell culture results better, we examined the biodegradation of the porous iron-manganese alloys in the cell culture medium. Unlike in the r-SBF medium (Fig. 6), hardly any biodegradation products were deposited even after 7 d and 28 d of immersion in the cell culture medium. This occurred due to the presence of serum in the cell culture medium [85,86], where metal ions were bonded by proteins [81,83], thus preventing the deposition of the biodegradation products. The struts of the scaffolds remained porous, almost identical to those in the as-sintered structures (**Fig. S7**). Undeniably, such a porous surface morphology allowed for rapid biodegradation (= more metal ion release), therefore inducing cytotoxicity. In earlier *in vivo* studies, iron-based biomaterials have been found to be systemically biocompatible [15,87–89], which is in agreement with our indirect cell culture results with a higher dilution ratio of the cell culture medium. Even so, other researchers have also found the evidence of *in vivo* local inflammation, caused by iron-based biomaterials [88,89]. Despite the existing *in vitro* cytotoxicity, the preosteoblasts extended filopodia (Fig. 10**b**) that may be due to the porous morphology of the struts and deposited calcium and phosphorus compounds as the biodegradation products (**Fig. S7**). Considering the much enhanced *in vitro* biodegradation rates of the porous iron-manganese alloys as compared to the biodegradation rate of pure iron, the obtained cytotoxicity results are not a surprise. Introducing a bioactive ceramic material into the iron-based scaffolds [90–92] will be

explored to improve the biocompatibility of the porous iron-based materials in order to meet all the requirements for ideal bone substitution.

5. Conclusions

We fabricated porous *ex situ*-alloyed iron-manganese scaffolds using extrusion-based 3D printing from elemental powders for the first time and characterized the *in vitro* properties of these materials for their intended use as bone substitutes. The scaffolds presented hierarchical interconnected pore networks with accurately controlled macropores and randomly distributed micropores. The addition of manganese to iron transformed the latter into a weakly paramagnetic material, which means these biomaterials can be classified as the first kind MRI-friendly biomaterials. The *in vitro* biodegradation rates of the porous iron-manganese alloys developed here are within the range of 0.18–0.23 mm/y after 28 d, as desired for ideal bone substitution. The mechanical properties of the porous iron-manganese scaffolds decreased over the *in vitro* biodegradation period of 28 d, but the strengths and elastic moduli remained in the range of the mechanical properties of the cancellous bone. The indirect cultures of preosteoblasts evidenced various levels of cytocompatibility of the porous iron-manganese alloys, depending on the dilution ratio of the extract. In the direct cultures, the cells showed their ability to attach to the scaffolds by developing numerous filopodia, but their viability was reduced by the presence of manganese and its associated effects on the scaffolds biodegradation. In conclusion, extrusion-based 3D printing is a viable multi-material additive manufacturing technique and, in combination with sintering, could deliver MRI-friendly porous iron-manganese biomaterials with significantly enhanced biodegradability and bone-mimicking mechanical properties as desired for bone substitutes.

Declaration of Competing Interest

The authors declare that they have no known competing financial interests or personal relationships that could have appeared to influence the work reported in this paper.

Acknowledgments

This work is part of the 3DMed project that has received the funding from the Interreg 2 Seas program 2014–2020, co-funded by the European Regional Development Fund under subsidy contract No. 2S04-014. The authors thank Mrs. Agnieszka Kooijman at the Department of Materials Science and Engineering, Delft University of Technology for her assistance in the electrochemical experiments. Mr. Ruud Hendrikx at the Department of Materials Science and Engineering, Delft University of Technology is acknowledged for the XRD analysis. Mr. Michel van den Brink at the Department of Process and Energy, Delft University of Technology is acknowledged for the ICP-OES analysis.

Supplementary materials

Supplementary material associated with this article can be found, in the online version, at doi:10.1016/j.actbio.2021.07.042.

References

[1] E. Roddy, M.R. DeBaun, A. Daoud-Gray, Y.P. Yang, M.J. Gardner, Treatment of critical-sized bone defects: clinical and tissue engineering perspectives, Eur. J. Orthop. Surg. Traumatol. 28 (2018) 351–362, doi:10.1007/s00590-017-2063-0.
[2] W. Wang, K.W.K. Yeung, Bone grafts and biomaterials substitutes for bone defect repair: a review, Bioact. Mater. 2 (2017) 224–247, doi:10.1016/j.bioactmat.2017.05.007.
[3] M.M. Stevens, Biomaterials for bone tissue engineering, Mater. Today 11 (2008) 18–25, doi:10.1016/S1369-7021(08)70086-5.
[4] S. Wu, X. Liu, K.W.K. Yeung, C. Liu, X. Yang, Biomimetic porous scaffolds for bone tissue engineering, Mater. Sci. Eng. R Rep. 80 (2014) 1–36, doi:10.1016/j.mser.2014.04.001.
[5] G.L. Koons, M. Diba, A.G. Mikos, Materials design for bone-tissue engineering, Nat. Rev. Mater. 5 (2020) 584–603, doi:10.1038/s41578-020-0204-2.
[6] K. Pałka, R. Pokrowiecki, Porous titanium implants: a review, Adv. Eng. Mater. 20 (2018) 1700648, doi:10.1002/adem.201700648.
[7] L.C. Zhang, L.Y. Chen, A review on biomedical titanium alloys: recent progress and prospect, Adv. Eng. Mater. 21 (2019) 1801215, doi:10.1002/adem.201801215.
[8] L. Tan, X. Yu, P. Wan, K. Yang, Biodegradable materials for bone repairs: a review, J. Mater. Sci. Technol. 29 (2013) 503–513, doi:10.1016/j.jmst.2013.03.002.
[9] Z. Sheikh, S. Najeeb, Z. Khurshid, V. Verma, H. Rashid, M. Glogauer, Biodegradable materials for bone repair and tissue engineering applications, Materials (Basel). 8 (2015) 5744–5794. 10.3390/ma8095273.
[10] Y.F. Zheng, X.N. Gu, F. Witte, Biodegradable metals, Mater. Sci. Eng. R. 77 (2014) 1–34, doi:10.1007/978-1-4614-3942-4_5.
[11] H.S. Han, S. Loffredo, I. Jun, J. Edwards, Y.C. Kim, H.K. Seok, F. Witte, D. Mantovani, S. Glyn-Jones, Current status and outlook on the clinical translation of biodegradable metals, Mater. Today 23 (2019) 57–71, doi:10.1016/j.mattod.2018.05.018.
[12] Y. Li, H. Jahr, J. Zhou, A.A. Zadpoor, Additively manufactured biodegradable porous metals, Acta Biomater. 115 (2020) 29–50, doi:10.1016/j.actbio.2020.08.018.
[13] J. He, F.L. He, D.W. Li, Y.L. Liu, Y.Y. Liu, Y.J. Ye, D.C. Yin, Advances in Fe-based biodegradable metallic materials, RSC Adv. 6 (2016) 112819–112838, doi:10.1039/C6RA20594A.
[14] R. Gorejová, L. Haverová, R. Oriňaková, A. Oriňak, M. Oriňak, Recent advancements in Fe-based biodegradable materials for bone repair, J. Mater. Sci. 54 (2019) 1913–1947, doi:10.1007/s10853-018-3011-z.
[15] T. Kraus, F. Moszner, S. Fischerauer, M. Fiedler, E. Martinelli, J. Eichler, F. Witte, E. Willbold, M. Schinhammer, M. Meischel, P.J. Uggowitzer, J.F. Löffler, A. Weinberg, Biodegradable Fe-based alloys for use in osteosynthesis: outcome of an *in vivo* study after 52 weeks, Acta Biomater. 10 (2014) 3346–3353, doi:10.1016/j.actbio.2014.04.007.
[16] L. Filli, R. Luechinger, T. Frauenfelder, S. Beck, R. Guggenberger, N. Farshad-Amacker, G. Andreisek, Metal-induced artifacts in computed tomography and magnetic resonance imaging: comparison of a biodegradable magnesium alloy versus titanium and stainless steel controls, Skelet. Radiol. 44 (2015) 849–856, doi:10.1007/s00256-014-2057-5.
[17] H. Hermawan, H. Alamdari, D. Mantovani, D. Dube, Iron-manganese : new class of metallic degradable biomaterials prepared by powder metallurgy, Powder Met. 51 (2008) 38–45, doi:10.1179/174329008X284868.
[18] Y. Ishikawa, Y. Endoh, Antiferromagnetism of γ-FeMn alloys, J. Appl. Phys. 39 (1968) 1318–1319, doi:10.1063/1.1656274.
[19] M. Schinhammer, A.C. Hänzi, J.F. Löffler, P.J. Uggowitzer, Design strategy for biodegradable Fe-based alloys for medical applications, Acta Biomater. 6 (2010) 1705–1713, doi:10.1016/j.actbio.2009.07.039.
[20] A. Yamamoto, R. Honma, M. Sumita, Cytotoxicity evaluation of 43 metal salts using murine fibroblasts and osteoblastic cells, J. Biomed. Mater. Res. 39 (1998) 331–340, doi:10.1002/(SICI)1097-4636(199802)39:2⟨331::AID-JBM22⟩3.0.CO;2-E.
[21] E. Zhang, H. Chen, F. Shen, Biocorrosion properties and blood and cell compatibility of pure iron as a biodegradable biomaterial, J. Mater. Sci. Mater. Med. 21 (2010) 2151–2163, doi:10.1007/s10856-010-4070-0.
[22] A.A. Zadpoor, Meta-biomaterials, Biomater. Sci. 8 (2020) 18–38, doi:10.1039/c9bm01247h.
[23] S.M. Ahmadi, R. Kumar, E.V. Borisov, R. Petrov, S. Leeflang, Y. Li, N. Tümer, R. Huizenga, C. Ayas, A.A. Zadpoor, V.A. Popovich, From microstructural design to surface engineering: a tailored approach for improving fatigue life of additively manufactured meta-biomaterials, Acta Biomater. 83 (2019) 153–166, doi:10.1016/j.actbio.2018.10.043.
[24] Q. Zhang, P. Cao, Degradable porous Fe-35wt.% Mn produced via powder sintering from NH_4NHCO_3 porogen, Mater. Chem. Phys. 163 (2015) 394–401, doi:10.1016/j.matchemphys.2015.07.056.
[25] Y.P. Feng, N. Gaztelumendi, J. Fornell, H.Y. Zhang, P. Solsona, M.D. Baró, S. Suriñach, E. Ibáñez, L. Barrios, E. Pellicer, C. Nogués, J. Sort, Mechanical properties, corrosion performance and cell viability studies on newly developed porous Fe-Mn-Si-Pd alloys, J. Alloy. Compd. 724 (2017) 1046–1056, doi:10.1016/j.jallcom.2017.07.112.
[26] M. Heiden, E. Nauman, L. Stanciu, Bioresorbable Fe–Mn and Fe–Mn–HA for orthopedic implantation: enhancing degradation through porosity control, Adv. Healthc. Mater. 6 (2017) 1–12, doi:10.1002/adhm.201700120.
[27] Y. Yin, Q. Huang, L. Liang, X. Hu, T. Liu, Y. Weng, T. Long, Y. Liu, Q. Li, S. Zhou, H. Wu, *In vitro* degradation behavior and cytocompatibility of ZK30/bioactive glass composites fabricated by selective laser melting for biomedical applications, J. Alloy. Compd. 785 (2019) 38–45, doi:10.1016/j.jallcom.2019.01.165.
[28] B. Liu, Y.F. Zheng, L. Ruan, *In vitro* investigation of Fe30Mn6Si shape memory alloy as potential biodegradable metallic material, Mater. Lett. 65 (2011) 540–543, doi:10.1016/j.matlet.2010.10.068.
[29] M. Schinhammer, P. Steiger, F. Moszner, J.F. Löffler, P.J. Uggowitzer, Degradation performance of biodegradable FeMnC(Pd) alloys, Mater. Sci. Eng. C 33 (2013) 1882–1893, doi:10.1016/j.msec.2012.10.013.

[30] Y.P. Feng, A. Blanquer, J. Fornell, H. Zhang, P. Solsona, M.D. Baró, S. Suriñach, E. Ibáñez, E. García-Lecina, X. Wei, R. Li, L. Barrios, E. Pellicer, C. Nogués, J. Sort, Novel Fe-Mn-Si-Pd alloys: insights into mechanical, magnetic, corrosion resistance and biocompatibility performances, J. Mater. Chem. B 4 (2016) 6402–6412, doi:10.1039/c6tb01951j.
[31] H. Hermawan, D. Dubé, D. Mantovani, Development of degradable Fe-35Mn alloy for biomedical application, Adv. Mater. Res. 15 (2007) 107–112, doi:10.4028/www.scientific.net/amr.15-17.107.
[32] M. Kupková, M. Hrubovčáková, M. Kupka, R. Oriňáková, Sintering behaviour, graded microstructure and corrosion performance of sintered Fe-Mn biomaterials, Int. J. Electrochem. Sci. 10 (2015) 9256–9268.
[33] M.S. Dargusch, A. Dehghan-Manshadi, M. Shahbazi, J. Venezuela, X. Tran, J. Song, N. Liu, C. Xu, Q. Ye, C. Wen, Exploring the role of manganese on the microstructure, mechanical properties, biodegradability, and biocompatibility of porous iron-based scaffolds, ACS Biomater. Sci. Eng. 5 (2019) 1686–1702, doi:10.1021/acsbiomaterials.8b01497.
[34] S.M. Huang, E.A. Nauman, L.A. Stanciu, Investigation of porosity on mechanical properties, degradation and *in-vitro* cytotoxicity limit of Fe30Mn using space holder technique, Mater. Sci. Eng. C 99 (2019) 1048–1057, doi:10.1016/j.msec.2019.02.055.
[35] P. Liu, D. Zhang, Y. Dai, J. Lin, Y. Li, C. Wen, Microstructure, mechanical properties, degradation behavior, and biocompatibility of porous Fe-Mn alloys fabricated by sponge impregnation and sintering techniques, Acta Biomater. 114 (2020) 485–496, doi:10.1016/j.actbio.2020.07.048.
[36] A.A. Zadpoor, Additively manufactured porous metallic biomaterials, J. Mater. Chem. B 7 (2019) 4088–4117, doi:10.1039/c9tb00420c.
[37] D.T. Chou, D. Wells, D. Hong, B. Lee, H. Kuhn, P.N. Kumta, Novel processing of iron-manganese alloy-based biomaterials by inkjet 3-D printing, Acta Biomater. 9 (2013) 8593–8603, doi:10.1016/j.actbio.2013.04.016.
[38] D. Hong, D.T. Chou, O.I. Velikokhatnyi, A. Roy, B. Lee, I. Swink, I. Issaev, H.A. Kuhn, P.N. Kumta, Binder-jetting 3D printing and alloy development of new biodegradable Fe-Mn-Ca/Mg alloys, Acta Biomater. 45 (2016) 375–386, doi:10.1016/j.actbio.2016.08.032.
[39] C. Shuai, W. Yang, Y. Yang, H. Pan, C. He, F. Qi, D. Xie, H. Liang, Selective laser melted Fe-Mn bone scaffold: microstructure, corrosion behavior and cell response, Mater. Res. Express. 7 (2019) 015404, doi:10.1088/2053-1591/ab62f5.
[40] D. Carluccio, C. Xu, J. Venezuela, Y. Cao, D. Kent, M. Bermingham, A.G. Demir, B. Previtali, Q. Ye, M. Dargusch, Additively manufactured iron-manganese for biodegradable porous load-bearing bone scaffold applications, Acta Biomater. 103 (2020) 346–360, doi:10.1016/j.actbio.2019.12.018.
[41] Y. Nie, G. Chen, H. Peng, S. Tang, Z. Zhou, F. Pei, B. Shen, *In vitro* and 48 weeks *in vivo* performances of 3D printed porous Fe-30Mn biodegradable scaffolds, Acta Biomater. 121 (2020) 724–740, doi:10.1016/j.actbio.2020.12.028.
[42] A.L. Rutz, K.E. Hyland, A.E. Jakus, W.R. Burghardt, R.N. Shah, A multimaterial bioink method for 3D printing tunable, cell-compatible hydrogels, Adv. Mater. 27 (2015) 1607–1614, doi:10.1002/adma.201405076.
[43] A.E. Jakus, S.L. Taylor, N.R. Geisendorfer, D.C. Dunand, R.N. Shah, Metallic architectures from 3D-printed powder-based liquid inks, Adv. Funct. Mater. 25 (2015) 6985–6995, doi:10.1002/adfm.201503921.
[44] N.E. Putra, M.J. Mirzaali, I. Apachitei, J. Zhou, A.A. Zadpoor, Multi-material additive manufacturing technologies for Ti-, Mg-, and Fe-based biomaterials for bone substitution, Acta Biomater. 109 (2020) 1–20, doi:10.1016/j.actbio.2020.03.037.
[45] N.E. Putra, M.A. Leeflang, M. Minneboo, P. Taheri, L.E. Fratila-Apachitei, J.M.C. Mol, J. Zhou, A.A. Zadpoor, Extrusion-based 3D printed biodegradable porous iron, Acta Biomater. 121 (2020) 741–756, doi:10.1016/j.actbio.2020.11.022.
[46] ASTM B963-17, Standard test methods for oil content, oil-impregnation efficiency, and surface-connected porosity of sintered powder metallurgy (PM) products using archimedes' principle, ASTM International, 2017. 10.1520/B0963-14.
[47] A. Oyane, H. Kim, T. Furuya, T. Kokubo, T. Miyazaki, T. Nakamura, Preparation and assessment of revised simulated body fluids, J. Biomed. Mater. Res. Part A 65 (2003) 188–195, doi:10.1002/jbm.a.10482.
[48] L. Yang, E. Zhang, Biocorrosion behavior of magnesium alloy in different simulated fluids for biomedical application, Mater. Sci. Eng. C 29 (2009) 1691–1696, doi:10.1016/j.msec.2009.01.014.
[49] ASTM G1-03Standard Practice for Preparing, Cleaning, and Evaluating Corrosion Test, ASTM International, 2017, doi:10.1520/G0001-03R11.
[50] ASTM G31-72Standard Practice for Laboratory Immersion Corrosion Testing for Metals, ASTM International, 2004, doi:10.1520/G0031-72R04.
[51] ISO 13314Mechanical Testing of Metals - Ductility Testing - Compression Test for Porous and Cellular Metals, International Organization for Standardization, 2011 ISO 13314:2011.
[52] ISO 10993-12Sample Preparation and Reference Materials, International Organization for Standardization, 2012, doi:10.1016/S0080-8784(08)60069-1.
[53] C. Shuai, S. Li, S. Peng, P. Feng, Y. Lai, C. Gao, Biodegradable metallic bone implants, Mater. Chem. Front. 3 (2019) 544–562, doi:10.1039/c8qm00507a.
[54] E.F. Morgan, G.U. Unnikrisnan, A.I. Hussein, Bone mechanical properties in healthy and diseased states, Annu. Rev. Biomed. Eng. 20 (2018) 119–143, doi:10.1146/annurev-bioeng-062117-121139.
[55] A. Šalak, M. Selecká, R. Bureš, Manganese in ferrous powder metallurgy, Powder Metall. Prog. 1 (2001) 41–58.
[56] J. Martínez, S.M. Cotes, A.F. Cabrera, J. Desimoni, A. Fernández Guillermet, On the relative fraction of ε martensite in γ-Fe-Mn alloys, Mater. Sci. Eng. A 408 (2005) 26–32, doi:10.1016/j.msea.2005.06.019.
[57] A. Rabinkin, On magnetic contributions to $\gamma \rightarrow \varepsilon$ phase transformations in Fe-Mn alloys, Calphad 3 (1979) 77–84, doi:10.1016/0364-5916(79)90008-7.
[58] M. Acet, T. Schneider, B. Gehrmann, E. Wassermann, The magnetic aspects of the γ-α and γ-ε martensitic transformations in Fe-Mn alloys, J. Phys. IV 5 (1995) C8–379, doi:10.1051/jp4.
[59] Z. Wang, C. Wang, C. Li, Y. Qin, L. Zhong, B. Chen, Z. Li, H. Liu, F. Chang, J. Wang, Analysis of factors influencing bone ingrowth into three-dimensional printed porous metal scaffolds: a review, J. Alloy. Compd. 717 (2017) 271–285, doi:10.1016/j.jallcom.2017.05.079.
[60] R. Wu, Y. Li, M. Shen, X. Yang, L. Zhang, X. Ke, G. Yang, C. Gao, Z. Gou, S. Xu, Bone tissue regeneration: the role of finely tuned pore architecture of bioactive scaffolds before clinical translation, Bioact. Mater. 6 (2021) 1242–1254, doi:10.1016/j.bioactmat.2020.11.003.
[61] H. Hermawan, D. Dube, D. Mantovani, Degradable metallic biomaterials : design and development of Fe–Mn alloys for stents, J. Biomed. Mater. Res. Part A 93 (2009) 1–11, doi:10.1002/jbm.a.32224.
[62] D. Bian, L. Qin, W. Lin, D. Shen, H. Qi, X. Shi, G. Zhang, H. Liu, H. Yang, J. Wang, D. Zhang, Y. Zheng, Magnetic resonance (MR) safety and compatibility of a novel iron bioresorbable scaffold, Bioact. Mater. 5 (2020) 260–274, doi:10.1016/j.bioactmat.2020.02.011.
[63] J.F. Schenck, The role of magnetic susceptibility in magnetic resonance imaging: MRI magnetic compatibility of the first and second kinds, Med. Phys. 23 (1996) 815–850, doi:10.1118/1.597854.
[64] K.M. Koch, B.A. Hargreaves, K.B. Pauly, W. Chen, G.E. Gold, K.F. King, Magnetic resonance imaging near metal implants, J. Magn. Reson. Imaging 32 (2010) 773–787, doi:10.1002/jmri.22313.
[65] P.M. Jungmann, C.A. Agten, C.W. Pfirrmann, R. Sutter, Advances in MRI around metal, J. Magn. Reson. Imaging 46 (2017) 972–991, doi:10.1002/jmri.25708.
[66] F.G. Shellock, Metallic neurosurgical implants: evaluation of magnetic field interactions, heating, and artifacts at 1.5-Tesla, J. Magn. Reson. Imaging 14 (2001) 295–299, doi:10.1002/jmri.1185.
[67] F.G. Shellock, S. Valencerina, Septal repair implants: Evaluation of magnetic resonance imaging safety at 3 T, Magn. Reson. Imaging 23 (2005) 1021–1025, doi:10.1016/j.mri.2005.10.010.
[68] L.N. Carter, O. Addison, N. Naji, P. Seres, A.H. Wilman, D.E.T. Shepherd, L. Grover, S. Cox, Reducing MRI susceptibility artefacts in implants using additively manufactured porous Ti-6Al-4V structures, Acta Biomater. 107 (2020) 338–348, doi:10.1016/j.actbio.2020.02.038.
[69] M. Schinhammer, I. Gerber, A.C. Hänzi, P.J. Uggowitzer, On the cytocompatibility of biodegradable Fe-based alloys, Mater. Sci. Eng. C 33 (2013) 782–789, doi:10.1016/j.msec.2012.11.002.
[70] E. Mouzou, C. Paternoster, R. Tolouei, A. Purnama, P. Chevallier, D. Dubé, F. Prima, D. Mantovani, *In vitro* degradation behavior of Fe-20Mn-1.2C alloy in three different pseudo-physiological solutions, Mater. Sci. Eng. C 61 (2016) 564–573, doi:10.1016/j.msec.2015.12.092.
[71] E. Mouzou, C. Paternoster, R. Tolouei, P. Chevallier, C.A. Biffi, A. Tuissi, D. Mantovani, CO_2-rich atmosphere strongly affects the degradation of Fe-21Mn-1C for biodegradable metallic implants, Mater. Lett. 181 (2016) 362–366, doi:10.1016/j.matlet.2016.06.017.
[72] C. Tonna, C. Wang, D. Mei, S.V. Lamaka, M.L. Zheludkevich, J. Buhagiar, Biodegradation behaviour of Fe-based alloys in hank's balanced salt solutions: part I. material characterisation and corrosion testing, Bioact. Mater. (2021), doi:10.1016/j.bioactmat.2021.05.048.
[73] C. Wang, C. Tonna, D. Mei, J. Buhagiar, M.L. Zheludkevich, S.V. Lamaka, Biodegradation behaviour of Fe-based alloys in hanks' balanced salt solutions: part II. the evolution of local pH and dissolved oxygen concentration at metal interface, Bioact. Mater. (2021), doi:10.1016/j.bioactmat.2021.05.014.
[74] X. Lu, Y. Leng, Theoretical analyze of calcium phosphate precipitation in simulated body fluid, Biomaterials 26 (2005) 1097–1108, doi:10.1016/j.biomaterials.2004.05.034.
[75] Y.S. Zhang, X.M. Zhu, S.H. Zhong, Effect of alloying elements on the electrochemical polarization behavior and passive film of Fe-Mn base alloys in various aqueous solutions, Corros. Sci. 46 (2004) 853–876, doi:10.1016/j.corsci.2003.09.002.
[76] M. Heiden, E. Walker, E. Nauman, L. Stanciu, Evolution of novel bioresorbable iron-manganese implant surfaces and their degradation behaviors *in vitro*, J. Biomed. Mater. Res. Part A 103 (2015) 185–193, doi:10.1002/jbm.a.35155.
[77] J. Venezuela, M.S. Dargusch, Addressing the slow corrosion rate of biodegradable Fe-Mn: current approaches and future trends, Curr. Opin. Solid State Mater. Sci. 24 (2020) 100822, doi:10.1016/j.cossms.2020.100822.
[78] J.A. Spencer, F. Ferraro, E. Roussakis, A. Klein, J. Wu, J.M. Runnels, W. Zaher, L.J. Mortensen, C. Alt, R. Turcotte, R. Yusuf, D. Côté, S.A. Vinogradov, D.T. Scadden, C.P. Lin, Direct measurement of local oxygen concentration in the bone marrow of live animals, Nature 508 (2014) 269–273, doi:10.1038/nature13034.
[79] P. Sotoudeh Bagha, M. Khakbiz, N. Safaie, S. Sheibani, S. Ebrahimi-Barough, Effect of high energy ball milling on the properties of biodegradable nanostructured Fe-35 wt.%Mn alloy, J. Alloy. Compd. 768 (2018) 166–175, doi:10.1016/j.jallcom.2018.07.261.
[80] ISO 10993-5Tests for *in vitro* Cytotoxicity, International Organization for Standardization, 2009, doi:10.1021/es0620181.
[81] R. Eid, N.T.T. Arab, M.T. Greenwood, Iron mediated toxicity and programmed cell death: a review and a re-examination of existing paradigms, Biochim. Biophys. Acta Mol. Cell Res. 1864 (2017) 399–430, doi:10.1016/j.bbamcr.2016.12.002.

[82] Y.F. He, Y. Ma, C. Gao, G.Y. Zhao, L.L. Zhang, G.F. Li, Y.Z. Pan, K. Li, Y.J. Xu, Iron overload inhibits osteoblast biological activity through oxidative stress, Biol. Trace Elem. Res. 152 (2013) 292–296, doi:10.1007/s12011-013-9605-z.
[83] P. Chen, J. Bornhorst, M. Aschner, Manganese metabolism in humans, Front. Biosci. Landmark 23 (2018) 1655–1679, doi:10.2741/4665.
[84] D. Carluccio, C. Xu, J. Venezuela, Y. Cao, D. Kent, M. Bermingham, A.G. Demir, B. Previtali, Q. Ye, M. Dargusch, Additively manufactured iron-manganese for biodegradable porous load-bearing bone scaffold applications, Acta Biomater. 103 (2020) 346–360, doi:10.1016/j.actbio.2019.12.018.
[85] V. Wagener, A.S. Faltz, M.S. Killian, P. Schmuki, S. Virtanen, Protein interactions with corroding metal surfaces: comparison of Mg and Fe, Faraday Discuss. 180 (2015) 347–360, doi:10.1039/c4fd00253a.
[86] R. Oriňaková, R. Gorejová, Z.O. Králová, A. Oriňak, I. Shepa, J. Hovancová, A. Kovalčíková, Z.L. Bujňáková, N. Király, M. Kaňuchová, M. Baláž, M. Strečková, M. Kupková, M. Hrubovčáková, F. Kaľavský, M. Oriňak, Influence of albumin interaction on corrosion resistance of sintered iron biomaterials with polyethyleneimine coating, Appl. Surf. Sci. 509 (2020) 145379, doi:10.1016/j.apsusc.2020.145379.
[87] M. Fântânariu, L.C. Trinc, C. Solcan, A. Trofin, S. E.V., S. Stanciu, A new Fe-Mn-Si alloplastic biomaterial as bone grafting material: *In vivo* study, Appl. Surf. Sci. 352 (2015) 129–139, doi:10.1016/j.apsusc.2015.04.197.
[88] Q. Feng, D. Zhang, C. Xin, X. Liu, W. Lin, W. Zhang, S. Chen, K. Sun, Characterization and *in vivo* evaluation of a bio-corrodible nitrided iron stent, J. Mater. Sci. Mater. Med. 24 (2013) 713–724, doi:10.1007/s10856-012-4823-z.
[89] M. Traverson, M. Heiden, L.A. Stanciu, E.A. Nauman, Y. Jones-hall, G.J. Breur, *In vivo* evaluation of biodegradability and biocompatibility of Fe30Mn alloy, Vet. Comp. Orthop. Traumatol. 31 (2018) 10–16.
[90] H. Ma, T. Li, Z. Huan, M. Zhang, Z. Yang, J. Wang, J. Chang, C. Wu, 3D printing of high-strength bioscaffolds for the synergistic treatment of bone cancer, NPG Asia Mater. 10 (2018) 31–44, doi:10.1038/s41427-018-0015-8.
[91] C. Shuai, Y. Li, Y. Yang, S. Peng, W. Yang, F. Qi, S. Xiong, H. Liang, L. Shen, Bioceramic enhances the degradation and bioactivity of iron bone implant, Mater. Res. Express. 6 (2019) 115401, doi:10.1088/2053-1591/ab45b9.
[92] C. Gao, M. Yao, S. Li, P. Feng, S. Peng, C. Shuai, Highly biodegradable and bioactive Fe-Pd-bredigite biocomposites prepared by selective laser melting, J. Adv. Res. 20 (2019) 91–104, doi:10.1016/j.jare.2019.06.001.